



Rivero, A. E., Cooper, J. E., & Woods, B. K. S. (2020). Numerically Efficient Three-Dimensional Fluid-Structure Interaction Analysis for Composite Camber Morphing Aerostructures. In *AIAA Scitech 2020 Forum* [2020-1298] American Institute of Aeronautics and Astronautics Inc. (AIAA). <https://doi.org/10.2514/6.2020-1298>

Peer reviewed version

Link to published version (if available):
[10.2514/6.2020-1298](https://doi.org/10.2514/6.2020-1298)

[Link to publication record in Explore Bristol Research](#)
PDF-document

This is the author accepted manuscript (AAM). The final published version (version of record) is available online via American Institute of Aeronautics and Astronautics at <https://arc.aiaa.org/doi/abs/10.2514/6.2020-1298>. Please refer to any applicable terms of use of the publisher.

University of Bristol - Explore Bristol Research

General rights

This document is made available in accordance with publisher policies. Please cite only the published version using the reference above. Full terms of use are available:
<http://www.bristol.ac.uk/pure/about/ebr-terms>

Numerically Efficient Three-Dimensional Fluid-Structure Interaction Analysis for Composite Camber Morphing Aerostructures

Andres E. Rivero*, Jonathan E. Cooper† and Benjamin K.S. Woods‡

Bristol Composites Institute (ACCIS), University of Bristol, Bristol, United Kingdom, BS8 1TR

This paper presents a newly developed three-dimensional Fluid-Structure Interaction (FSI) routine for the Fish Bone Active Camber (FishBAC) concept that couples a three-dimensional Lifting-Line theory analysis to a two-dimensional viscous corrected panel method (XFOIL) to create a viscous corrected three-dimensional wing aerodynamic solver. This aerodynamic model is then coupled to a previously developed multi-component Mindlin-Reissner plate model based composite analysis routine for the FishBAC morphing device. The methodology is explained, and predictions are validated against existing modeling tools. The FSI model developed in this paper shows good agreement when compared against other structural, aerodynamic and FSI tools. Additionally, results show the FishBAC's ability to improve aerodynamic performance at a wide range of operating conditions.

I. Nomenclature

Roman symbols (uppercase)

\bar{Q}_{ij}	ply stiffness in the global coordinate system
C_D	3D drag coefficient
C_L	3D lift coefficient
C_{D_0}	3D profile drag coefficient
C_{D_i}	3D induced drag coefficient
$C_{L_{err}}$	FSI convergence criterion
C_m	3D pitching moment coefficient
DF	damping factor
H_{ij}	transverse shear stiffness matrix terms
L'	lift per unit span
L_{mn}, O_{mn}, P_{mn}	displacements shape functions' unknown amplitudes
P	aerodynamic pressure distribution
R_{mn}, S_{mn}	rotations shape functions' unknown amplitudes
T	kinetic energy
U_p	artificial penalty energy
V, W	potential energy due to transverse and in-plane external loads, respectively
V_∞	freestream velocity
V_{eff}	effective velocity

*PhD Student, Bristol Composites Institute (ACCIS), Department of Aerospace Engineering. AIAA Student Member.

†RAEng Airbus Sir George White Professor of Aerospace Engineering, Department of Aerospace Engineering. AIAA Fellow.

‡Lecturer in Aerospace Structures, Bristol Composites Institute (ACCIS), Department of Aerospace Engineering. AIAA Member.

$X(x)$	Chebyshev polynomial expansion in the x -direction
$Y(y)$	Chebyshev polynomial expansion in the y -direction
Roman Symbols (lowercase)	
\hat{c}	unit-vector parallel to local chord
\hat{n}	unit-vector perpendicular to local chord
\vec{n}	normal vector at horseshoe control point
\vec{r}	spatial position vectors
c	chord length
c_l	2D lift coefficient
c_{d0}	2D profile drag coefficient
c_m	2D pitching moment coefficient
f_{mn}	influence coefficients
k_k	artificial penalty spring stiffness
q	net aerodynamic pressure distribution
q^r	under-relaxed net aerodynamic pressure distribution
u_{ij}^o	in-plane displacement in the chordwise x -direction
v_{ij}^o	in-plane displacement in the spanwise y -direction
w^r	under-relaxed transverse displacement
w_{ij}	out-of-plane displacement in the through-thickness z -direction
Greek symbols	
α	geometric angle of attack
α_{eff}	effective angle of attack
α_i	induced angle of attack
ϵ	strains
η_j	normalized spanwise position
Γ	vortex strength
$\gamma(\text{TE})$	Kutta condition
$\gamma_{xy}, \gamma_{xz}, \gamma_{yz}$	engineering shear strains
Γ_x	boundary conditions circulation function
κ	Timoshenko shear correction factor
λ	FSI relaxation factors
ϕ	velocity potential
Π	total potential energy
ψ_x	xz -plane rotation
ψ_y	yz -plane rotation
ρ_∞	freestream air density
σ	normal stress
τ	shear stress
$T_n(\zeta)$	Chebyshev polynomials of the first kind
θ	local twist angle
ζ_i	normalized chordwise position

II. Introduction

FIXED-WING aircraft are typically controlled and manoeuvred using deflectable, discrete structures that are hinged to the trailing edge of the wings. These hinged panels are generally known as control surfaces and, depending on their location, these are specifically known as ailerons, elevator and rudder. Also, they are generally known as trailing edge flaps. When deflected, these discrete flaps vary the camber of the airfoil, and therefore the pressure distribution over the wing, resulting in net aerodynamic forces and moments that can be used to control the lift generation and orientation of the aircraft. Although effective in generating these net forces and moments for control purposes, their use comes with a drag penalty due to the sharp and discontinuous change in shape, which promotes flow separation and increases wake turbulence [1]. Alternatively, if these control surfaces could instead deflect and change shape in a smooth and continuous way, similar control capabilities could be achieved, but with a lower drag penalty. This alternative is known as camber morphing, and previous studies have estimated a potential fuel consumption reduction between 3% and 6% if implemented in fixed-wing aircraft [2].

Furthermore, the ability to vary wing geometry continuously and throughout the entire flight could lead to important fuel efficiency gains. Airplanes continuously lose weight during flight due to fuel burn, hence, the amount of lift required to sustain equilibrium flight is continuously changing. Therefore, optimum lift-to-drag ratios cannot be achieved throughout the entire flight if wing geometries are not continuously adapted. Consequently, the ability to vary camber distribution during flight can be exploited to achieve higher lift-to-drag ratios at the different flight stages. Recksieck (2009) estimated that fuel consumption could be reduced between 1-2% in a full size Airbus A350 XWB if traditional hinged ailerons are actively used to maximise aerodynamic efficiency [3]. Therefore, these fuel efficiency gains due to active use of ailerons during flight could be even higher with camber morphing.

Even though the aeronautical community has been aware of the benefits of camber morphing for almost a century—as the first camber morphing concepts date from as early as 1920 [4–6]—it is only in the past two decades that these concepts have started to be considered as feasible alternatives to rigid control surfaces. This has been partly due to new developments in smart materials and lightweight structures and advancements in structural modeling, which have allowed researchers to develop new morphing concepts [7]. For example, developments in piezoelectric materials [8, 9] and Shape-Memory Alloys (SMA) [10, 11] have focused on exploring alternative actuation mechanisms, whereas further understanding of composite laminates have led to exploiting structural instabilities for shape changing [12–14]. However, most of these research efforts have essentially focused on 2-D morphing airfoils, and not necessarily on their integration into three-dimensional wings—from a systems level point-of-view, and the potential benefits and complications this may bring.

Conversely, some research efforts did focus on the benefits of morphing from a fixed-wing aircraft systems level point-of-view. Few of these cases are the NASA Ames F-111 Mission Adaptive Wing [15] and the DARPA Smart Wing project [16], whereas other researchers have studied the aeroelastic implications of camber morphing [17].

To successfully implement camber morphing concepts in fixed-wing applications, it is necessary to address both the two-dimensional airfoil lightweight morphing concept design, as well as its integration in three-dimensional wings, simultaneously. However, there is a current lack of these combined efforts in the literature. The modeling tools developed in this paper, along with previous work on the design, manufacture and test of a composite Fish Bone Active Camber (FishBAC) morphing wing [18, 19], aim to address this literature gap. These modeling tools can be used to further understand the structural and aerodynamic behavior of the FishBAC, as well as for future design iterations and optimization of composite FishBAC wings.

III. Fish Bone Active Camber (FishBAC) Concept

The Fish Bone Active Camber (FishBAC) [20] is a compliance-based camber morphing device that has been carefully engineered to have high stiffness in certain desired directions—i.e. along the span, to resist bending—while being compliant in thicknesswise bending to allow camber morphing (Fig. 1). The latest FishBAC prototype achieves this high-level of anisotropy by combining several types of structural members and materials, such as a carbon-fibre/epoxy bending spine (main load bearing member), spanwise stringers, silicone skin sheets and a pair of Kevlar-tape tendons for transferring actuation loads [18] (Fig. 2). Since the FishBAC is actuated at different locations along the span—two locations on the latest composite prototype—it has the ability to achieve gradual changes in camber along the spanwise direction. From a 3D wing design perspective, this creates the exciting possibility of using the FishBAC to control spanwise aerodynamic loads in real time. This could allow for more efficient flight through a number of means. The ability to control spanwise lift distribution with smooth camber variation along the chord and span would allow to minimize both profile drag and induced drag in all flight conditions.

The lack of gaps or sudden spanwise changes in camber seen with flap based systems would further increase the achievable drag reductions. Additionally, continuous control of wing camber, given sufficient actuation bandwidth, would allow for the additional functionality of gust load alleviation—which could lead to lighter and higher aspect ratio wings. Such a fully morphing camber wing would retain the structural efficiency and practical benefits (e.g. fuel storage) of a traditional wingbox structure by modifying only the trailing edge, while opening up a whole new level of operational freedom and responsiveness beyond what is achievable with traditional approaches.

To properly exploit all the benefits that the FishBAC can bring to a 3D wing, it is necessary to design and optimise the structure with the appropriate modeling tools that capture the complex structural configuration of the composite FishBAC, the 3D aerodynamics of a camber morphing 3D wing and the coupled aeroelastic behavior that these compliance-based morphing structures are intrinsically beholden to. Additionally, these modeling tools must be computationally efficient and with an appropriate level of fidelity to capture enough of the underlying physics to be usefully accurate while also being computationally efficient enough to be useful for expansive design and optimisation studies.

Previous work by the authors has advanced this aim through recent structural modeling work and prototype development. Recently developed structural models can predict the static structural behavior of the composite FishBAC [19, 21] using a reduced number of Degrees of Freedom (DOFs) compared to Finite Element Method (FEM). Additionally, these structural models were used to design a composite FishBAC wind tunnel wing model [18]. This composite prototype underwent a series of structural and wind tunnel tests to first experimentally study the behavior of the composite FishBAC and then use these experimental results to validate the modeling techniques. Given recent progress, it is now of necessary to develop an aerodynamic model that adequately predicts the 3D aerodynamic behavior of a 3D camber morphing wings, and to couple the structural and aerodynamic models together in a fluid-structure interaction (FSI) routine. This work is intended to create a self-contained, comprehensive analysis tool to significantly expand our understanding of the complex, coupled performance of fully camber morphing wings such that the potential benefits may be explored.

This paper presents this newly developed fluid-structure interaction (FSI) routine for three-dimensional camber morphing wings, including a detailed explanation of the aerodynamic model, a summary of the structural model, and description of the coupling procedure. This is followed by an initial investigation into the design space of camber morphing wings and presentation of achievable aerodynamic benefits for a case study.

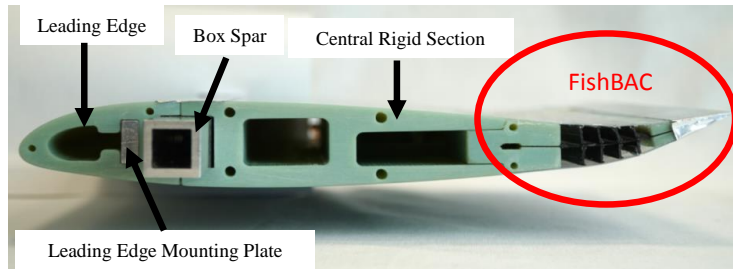


Fig. 1 Fish Bone Active Camber (FishBAC) morphing trailing edge device wind tunnel wing model

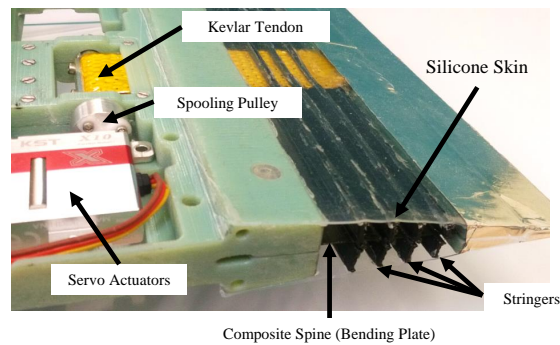


Fig. 2 FishBAC structure and actuation mechanism

IV. Fluid-Structure Interaction of Morphing Aerostructures: Background

Fluid-Structure Interaction models combine the interaction of a deformable body with the surrounding fluid flow. They are classified as either one-way or two-way routines; the former one occurs when the structural deformation affects the fluid motion—but not vice versa—whereas the latter refers to routines where both structural deformations and fluid motion affect each other [22].

Additionally, FSI routines can be classified into explicit and implicit algorithms. On one hand, explicit algorithms (also known as loosely-coupled) consist of separate structural and aerodynamic models which are coupled and then iterated until a converge solution is achieved. On the other hand, implicit algorithms (also known as strongly-coupled) find the converged solution using a single model that simultaneously accounts for both the structure and the aerodynamics [22]. Although strongly-coupled algorithms are generally more stable, they may be difficult to program and implement as both structures and aerodynamics solvers may require significant modification to combine them in a single system of equations [23]. Conversely, loosely-coupled algorithms may not be as stable, but their main advantage is that they allow the combination of previously developed efficient and stable independent structural and aerodynamic solvers.

In the morphing wings context—where aerostructures are subjected to large changes in shape—it is of extreme importance to develop two-way FSI routines since large changes in shape trigger significant aerodynamic changes, and vice versa. Failing to perform FSI analysis in morphing wings may lead to structural failure under aerodynamic loads, incorrect actuation sizing, structural overdesign and incorrect performance predictions, among others. There are several examples in literature of FSI routines for variable camber applications. Most of these models are based on loosely-coupled routines that used Finite Element Method (FEM) and Computational Fluid Dynamics (CFD) solvers for structures and aerodynamics, respectively. There are also examples in the literature of successful implementation of lower fidelity techniques to these sorts of problems.

1. CFD/FEM-based models

Krawczyk *et al.* developed a model based on FEM and CFD for camber morphing wind turbine blades for a generic camber morphing concept, which is then used to obtain aerodynamic forces and moments. However, no specific metrics to assess computational efficiency and convergence are provided [24]. Similarly, Macphee and Beyene developed a loosely-coupled model for morphing wind turbine blades, which is based on OpenFoam's CFD solver with a FEM-based finite strain analysis as structural solver. One of the main findings in this study is the potential use of camber morphing as passive pitch control mechanisms. Once again, no specific morphing concept is used in the analysis, and no measure of computational efficiency is performed [25].

Some authors have developed two-dimensional FSI models for specific camber morphing concepts. For example, Oehler *et al.* [26] performed an ABAQUS-based CFD and FEM analysis for Shape Memory Alloy (SMA) morphing devices. Similarly, Heo *et al.* [27] followed a similar approach—using ANSYS instead—for a compliance-based camber morphing cellular structures. Moreover, Barlas and Akay [28] also developed a 2D FEM and CFD-based algorithm using ANSYS solvers for optimisation of a morphing flap.

There has also been developments on FSI modeling of three-dimensional wings. For example, De Gaspari *et al.* [29] identified the need to study camber morphing at the 3D wing level, and therefore developed a model based on 3D CFD and 3D FEM. Miller *et al.* [30] also developed a FEM/CFD routine for variable camber wings, which also implemented a 3D interpolate algorithm to handle the dissimilar meshes used for structural versus aerodynamic analysis. After experimental validation, it was determined that the FSI model tends to under-predict lift coefficients and trailing edge displacements, and they suggest that a mesh refinement in both FEM and CFD models may improve results. Finally, Fasel *et al.* [31] also implements a 3D CFD and 3D FEM FSI analysis to model the aeroservoelasticity of a morphing airplane for energy harvesting.

In summary, all these FSI models focus on using CFD and FEM as structural and aerodynamic solvers, respectively. Even though this is a workable solution that is capable of finding converged solutions, their computational expense is significant, and geometry definition and meshing remain significant challenges in the context of design space exploration. While CFD and FEM can provide very meaningful levels of insight into the detailed aeromechanics of morphing, these two modeling techniques are not an ideal starting point if wing ranging explorations into the design space of 3D morphing wings are desired. A natural solution is to start with a lower fidelity of analysis to reduce computational expense, and to do so within a parametric design framework to allow for very quick changes in geometry and operating conditions.

2. Lower-Fidelity Models

There are two relevant examples of lower fidelity FSI models for camber morphing devices. First, Daynes and Weaver [32] developed a fluid-structure interaction model for a composite bistable camber morphing trailing edge device. Even though the authors did use FEM as structural solver, XFOIL—a 2D viscous-corrected panel method for two-dimensional airfoil analysis—was used to obtain the aerodynamic loads. Results showed that XFOIL provides sufficient aerodynamic information for validation of 2D wind tunnel test data, and a much lower computational expense than CFD.

Furthermore, Woods *et al.* [33] went one step further in reducing computational expense by also using XFOIL as aerodynamic solver, but by replacing FEM by an analytical Euler-Bernoulli beam theory structural model. This FSI routine was developed for the FishBAC device specifically, and represents a fast and inexpensive routine for two-dimensional airfoil analysis, design and optimisation of the FishBAC. For example, due to its efficiency, this FSI model was used for a multi-objective optimisation study of the FishBAC [34]. However, this model cannot be used for three-dimensional wing analysis as it is a two-dimensional model with no ability to handle the structural or aerodynamic impact of variations along the span.

From this brief review of relevant literature, it can be seen that a fully three-dimensional, computationally efficient FSI routine is needed to analyze, design and optimise composite FishBAC camber morphing wings. This new model will allow for a more thorough exploration into the aerodynamic performance of camber morphing wings than what has been achieved to date, and can be used to identify regions of the design space where higher fidelity analysis and wind tunnel testing should be targeted.

V. 3D FSI for Composite FishBAC Wings

A three-dimensional FSI routine for modeling the aeroelastic behavior of a composite FishBAC is proposed in this section. From the aerodynamics point-of-view, this model must be able account for local changes in 2D airfoil shapes due to varying camber, as well as for 3D aerodynamic effects. From the structures point-of-view, it needs to capture the stiffness discontinuities of the FishBAC, the use of different types of materials—including composite laminates—and the chordwise taper due to the airfoil geometry. Since a stable and efficient structural solver has already been developed [19], a loosely-coupled approach will be implemented. The following section describes the modeling techniques implemented to address these requirements.

A. Aerodynamic Model

One feasible option to fully capture the 3D aerodynamics of a finite wing is to use 3D panel methods, which discretize the outer surface of the wing into a series of chordwise and spanwise panels, hence capturing local changes in airfoil shape and thickness effects [35]. Although panel methods are significantly more efficient than CFD, it is difficult to incorporate viscosity effects into them, and viscous effects are an important contributor to the overall drag. Another option is to use numerical methods that are based on Prandtl’s Lifting-Line Theory, such as Vortex Lattice Method (VLM) [36] and its precursor, Weissinger Lifting-Line Theory (LLT) [37]. These two techniques implement finite vortex filaments to calculate lift and induced drag. Although these methods are very computationally efficient, they still neglect viscosity and do not capture airfoil thickness effects as they place the vortex filaments along the airfoil camber line. Hence, LLT and VLM are able to neither predict stall nor obtain accurate pressure distributions due to local changes in airfoil geometry.

An alternative approach to LLT that addresses the viscosity and thickness effects limitations is to couple the 3D lift distribution from LLT to 2D airfoil data that can be obtained from either experiments [38, 39] or a 2D-airfoil analysis tool [40], followed by iterating the 2D and 3D solutions until certain convergence criterion is met. Anderson *et al.* successfully implemented this technique for modeling the stall behavior of finite wing with drooped leading edge [39]. Their model coupled Prandtl’s LLT with 2D airfoil experimental data. They concluded that their coupled model had a maximum percentage difference of 20%, when compared to experimental data. However, the authors noted that it is important to be aware that LLT theory can be inaccurate at high angles of attack due to the flow becoming highly three-dimensional. An appropriate three-dimensional solver should be used for such cases.

Furthermore, Şugar-Gabor *et al.* implemented both LLT [41] and VLM [40] routines using XFOIL as two-dimensional flow solver. Their LLT was validated against CFD for Mach numbers between $M = 0.05$ and $M = 0.2$ and angles of attack between $\alpha = -2^\circ$ and $\alpha = +8^\circ$. They observed good agreement between CFD and LLT lift and pitch moment coefficients, however, drag coefficients start to diverge at angles of attack greater than $\alpha = 4^\circ$.

Also, they suggested in their VLM study that drag accuracy could be improved by introducing experimental results to the VLM+XFOIL algorithm [40]. Additionally, they tested their model to study the aerodynamics of a morphing wing, and were successfully able to quantify the aerodynamic performance gains of their morphing concept.

In summary, a LLT model with viscous corrections is a suitable approach for modeling the FishBAC's 3D aerodynamics at an appropriate level of fidelity for use in design space exploration and initial optimisation work. However, it is important to treat results at high angles of attack with care, as these may be inaccurate due to LLT's limitations on modeling fully 3D flows.

1. Weissinger's Lifting-Line Method

The Weissinger's Lifting-Line Method is a numerical modeling tool used to calculate the local downwash and effective angle of attack of a finite wing. It is considered to be a nonlinear extension of Prandtl's Lifting-Line Theory as it combines LLT with nonlinear airfoil section data. Thus, unlike Prandtl's LLT, the Weissinger's nonlinear LLT can be used to predict aerodynamic nonlinearities at stall. Moreover, LLT assumes that a finite wing can be replaced by spanwise vortex filaments (bound vortex) of variable strength along the span and a series of trailing edge vortices. The main bound vortex filaments local strengths $\Gamma(y)$ can be related to the local lift per unit span through the Kutta-Joukowski Theorem, which states that the lift per unit span can be calculated by knowing the vortex strength and the local freestream flow conditions, such that

$$L' = \rho_\infty V_\infty \Gamma(y). \quad (1)$$

The main purpose of the trailing edge vortices is to induce downwash velocities, which are then used to calculate the effective angles of attack [39]. Each set of one finite bound vortex—located at the each panel's quarter-chord—and two trailing edge vortices is known as a horseshoe vortex element (Fig. 3).

To implement Weissinger's Lifting-Line Method, the wing is partitioned into a number of spanwise elements, with each one containing a horseshoe vortex. In terms of chordwise elements, the Lifting-Line Method uses only one element along the chord. This is the main difference between Weissinger's Lifting-Line Method and Vortex Lattice Method, where horseshoe vortices are also used, but with multiple chordwise elements. In both techniques, the bound vortices are placed at the quarter-chord, whereas a control point is set at the three-quarter chord of each element. Each horseshoe vortex induces a velocity at each control point, which can be calculated using Biot-Savart Law

$$dV = \frac{\Gamma}{4\pi} \frac{d\vec{l} \times \vec{r}}{|\vec{r}|^3}. \quad (2)$$

For each horseshoe element, the induced velocity at a given point is given by the sum of the induced velocity from the bound vortex

$$V_{AB} = \frac{\Gamma}{4\pi} \frac{\vec{r}_1 \times \vec{r}_2}{|\vec{r}_1 \times \vec{r}_2|^2} \left[\vec{r}_0 \left(\frac{\vec{r}_1}{|\vec{r}_1|} - \frac{\vec{r}_2}{|\vec{r}_2|} \right) \right] \quad (3a)$$

and the two semi-infinite trailing edge vortices

$$V_{A\infty} = \frac{\Gamma}{4\pi} \left\{ \frac{r_{1k}\hat{j} - r_{1j}\hat{k}}{(r_{1k})^2 + (-r_{1j})^2} \right\} \left[1 + \frac{r_{1i}}{|\vec{r}_1|} \right] \quad \text{and} \quad V_{B\infty} = \frac{\Gamma}{4\pi} \left\{ \frac{r_{2k}\hat{j} - r_{2j}\hat{k}}{(r_{2k})^2 + (-r_{2j})^2} \right\} \left[1 + \frac{r_{2i}}{|\vec{r}_2|} \right]. \quad (3b)$$

where \vec{r}_0 , \vec{r}_1 and \vec{r}_2 defined the geometric position of each horseshoe vortex with respect to each control point. Fig. 4 shows a horseshoe element with its respective control point and the position vectors \vec{r}_0 , \vec{r}_1 and \vec{r}_2 .

Once all the induced velocities have been calculated using Eq. (3), a system of linear equations can be set to solve for the horseshoe vortex strengths. These vortex strengths are assumed to be uniform across the horseshoe. One boundary condition needs to be satisfied: the zero normal flow at each control point, defined as

$$\Delta(\Phi + \Phi_\infty) \cdot \vec{n} = 0, \quad (4)$$

where Φ refers to the potential of the freestream flow, Φ_∞ represents the potential from the induced velocities by the horseshoe elements and \vec{n} is the normal vector to each control point at the three-quarter-chord of each element.

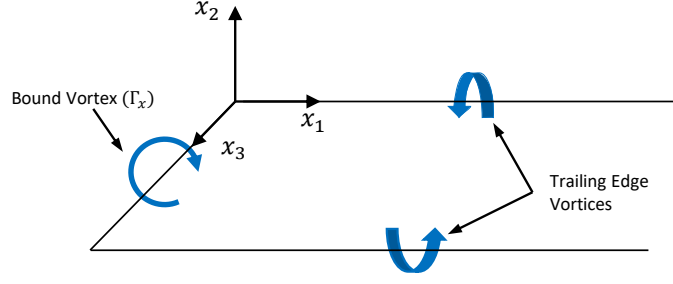


Fig. 3 Horseshoe vortex diagram. Reproduced from Chadwick [42] with author's permission

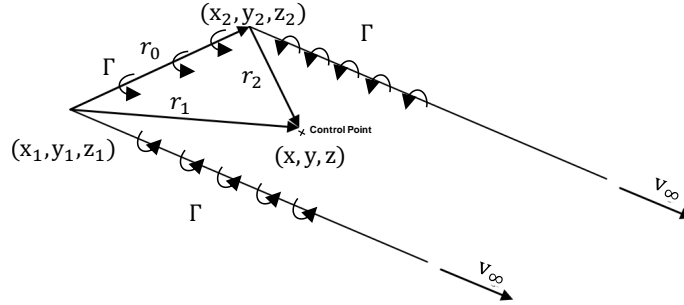


Fig. 4 Diagram of a horseshoe element with its respective position vectors and control point location. Reproduced from Şugar-Gabor *et al.* [41], with author's permission

This normal vector can be expressed in terms of the local twist angle (θ), wing dihedral (ϕ) and the local camber line slope (dz/dx), such as

$$\vec{n} = \sin\left(\theta - \frac{dz}{dx}\right) \cos(\phi) \hat{i} + \sin(\phi) \hat{j} + \cos\left(\theta - \frac{dz}{dx}\right) \cos(\phi) \hat{k}. \quad (5)$$

This zero normal flow at control points is applied by setting the sum of the freestream velocity and the induced velocities equal to zero, along the normal direction

$$[(V_{AB} + V_{A\infty} + V_{B\infty}) + V_{\infty}] \cdot \vec{n} = 0. \quad (6)$$

Finally, Eq. (3) can be substituted into Eq. (6) to obtain a system of $1 \times N$ equations—where N corresponds to the number of spanwise horseshoe elements—of the form

$$[f_{mn}][\Gamma_n] = [-V_{\infty} \cdot \vec{n}], \quad (7)$$

where f_{mn} are known as the influence coefficients [40, 43]. The calculated vortex strengths can then be used to calculate the lift-per-unit span at each horseshoe element by using Kutta-Joukowski theorem. However, these still need to be corrected for viscosity, which will be introduced in the following section. Finally, the effective angle of attack can be calculated at each spanwise element using the expression

$$\alpha_{\text{eff}_n} = \tan^{-1} \left(\frac{\vec{V}_{\text{eff}} \cdot \hat{n}}{\vec{V}_{\text{eff}} \cdot \hat{c}} \right), \quad \text{where} \quad \vec{V}_{\text{eff}} = \vec{V}_{\infty} + V_{A\infty} + V_{B\infty}. \quad (8)$$

This effective angle of attack is calculated at the local wing plane [44] and, therefore, the freestream vector and the chordwise and normal-to-chord unit vectors are defined as

$$\vec{V}_{\infty} = V_{\infty} (\cos \alpha \hat{i} + \sin \alpha \hat{k}), \quad \text{where} \quad \hat{n} = \hat{k} \quad \text{and} \quad \hat{c} = \hat{i}. \quad (9)$$

2. Viscous Corrected 2D Panel Method (XFOIL)

XFOIL is a two-dimensional panel method for airfoil analysis. It is based on the principle of potential flow theory, where the flowfield around an airfoil is constructed by superimposing the freestream flow, a vortex sheet and source sheet around the airfoil surface. The airfoil surface is discretized in a series of N flat panels, each one with unknown and uniform vortex and source strengths— γ_N and σ_N , respectively [45]. These unknown vortex and source strengths can then be found by setting up a system of equations using potential flow theory, and by applying the Kutta Condition as boundary condition. This condition states that the vortex strength at a sharp trailing edge must be zero, i.e. $\gamma(\text{TE}) = 0$. XFOIL corrects for viscosity by implementing a viscous boundary layer solver that models skin friction drag and flow separation based on the wall transpiration concept [45, 46].

As an open source code, XFOIL has been widely used for two-dimensional airfoil analysis under low freestream speeds and Reynolds number condition [45]. In terms of inputs, XFOIL requires the non-dimensional airfoil coordinates, the angle of attack, Mach number and Reynolds number to be provide. To obtain the airfoil coordinates, the wing is divided in two sections: the non-morphing rigid section and the FishBAC section, between non-dimensional chord locations of 0 to 0.744 and 0.744 to 1, respectively. For the non-morphing section, the coordinates are obtained by using the NACA 5-digit airfoil generator equations [47] and for the FishBAC morphing section, the airfoil shape is generated by fitting a sixth-order polynomial to the deformed FishBAC spine displacement field—obtained from the structural model. After each XFOIL run, a set of 2D aerodynamic coefficients and pressure distributions (top and bottom surfaces) are obtained.

3. Nonlinear Lifting-Line Solution

The use of nonlinear section lift data to enhance Lifting-Line Theory was first introduced by Sivells and Neely [38], describing this method as an alternative to estimate maximum lift coefficients of high aspect ratio and unswept wings. Furthermore, Anderson *et al.* [39] applied this technique to model drooped leading-edge wings. Anderson *et al.* described the procedure as follows: first, the nonlinear Lifting-Line Model is used to calculate the effective angle of attack at each panel, and with that initial effective angle of attack distribution, local lift coefficients can be interpolated from 2D airfoil data, be it experimental data, or in this work XFOIL results. With those interpolated lift coefficients, the lift per unit-span can be calculated at each horseshoe element using the lift equation

$$L' = \frac{1}{2} \rho_{\infty} V_{\infty}^2 c_n(y) c_l, \quad (10)$$

where c_n corresponds to the local airfoil chord length and c_l is the 2D lift coefficient. If the lift equation and Kutta-Joukowski theorem are combined, a local circulation from the 2D airfoil data can be calculated as

$$L' = \frac{1}{2} \rho_{\infty} V_{\infty}^2 c_n(y) c_l = \rho_{\infty} V_{\infty} \Gamma_{\text{new}}, \quad \text{where} \quad \Gamma_{\text{new}} = \frac{V_{\infty} c(y) c_l(y)}{2}. \quad (11)$$

The second step is to calculate the lift per unit-span at each horseshoe element from LLT. Using the bound vortex strength distribution previously obtained (Eq. (7)), the lift per unit-span at each horseshoe element can be calculated using Kutta-Joukowski theorem. These two different estimates of the vortex strength distribution are used to generate the next iteration's vortex strengths, such that

$$\Gamma_{n+1} = \Gamma_{\text{old}} + DF(\Gamma_{\text{new}} - \Gamma_{\text{old}}). \quad (12)$$

With this new vortex strength distribution, a new effective angle of attack distribution can be calculated, followed by another set of interpolations from 2D airfoil data. The process is repeated until a specified convergence criterion is met. In this application, the convergence criterion is a 0.5% difference between iterations. The use of a fixed relaxation factor is introduced to assist convergence. Previous studies have determined a value of $DF = 0.05$ is sufficient to assist convergence [37, 39], however, these studies noted that this relaxation factor is highly dependant on the specific geometry and operating condition. Due to large changes in camber in this application, it was observed that additional damping was needed to assist convergence. Therefore, a value of $DF = 0.001$ is used in this FSI model. Lastly, once a converged vortex strength distribution is obtained, a converged set of pressure distributions is interpolated from the 2D airfoil data. This pressure distribution is then applied to the structural model, which will be presented in the following section. A diagram of the aerodynamic model is presented in Fig. 5.

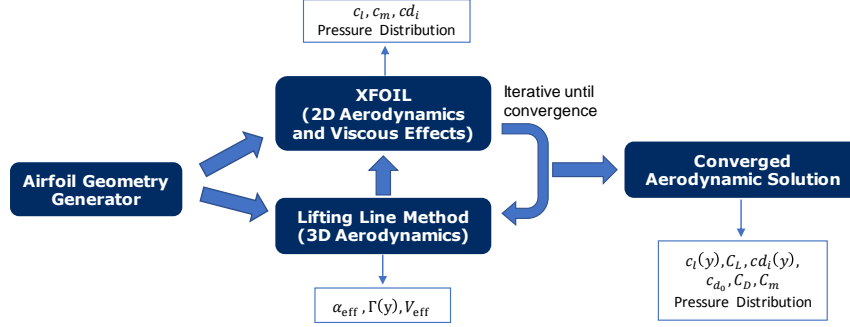


Fig. 5 Aerodynamic model convergence diagram

4. Aerodynamic Coefficients

Once a converged set of vortex strength distributions is obtained, the total lift coefficient and induced drag due to lift are calculated using the following expressions:

$$C_L = \frac{2}{V_\infty S} \int_{-b/2}^{b/2} \Gamma(y) dy \quad \text{and} \quad C_{D_i} = \frac{2}{V_\infty S} \int_{-b/2}^{b/2} \Gamma(y) \sin(\alpha_i) dy. \quad (13)$$

Additionally, the profile drag and pitching moment coefficients can be integrated from the interpolated XFOIL results, such that:

$$C_{D_0} = \int_{-b/2}^{b/2} c_{d_0}(y) dy \quad \text{and} \quad C_m = \int_{-b/2}^{b/2} c_m(y) dy. \quad (14)$$

Finally, the total drag coefficient is defined as the sum of profile and induced drag coefficients, defined as

$$C_D = C_{D_0} + C_{D_i}. \quad (15)$$

B. Structural Model

The structural model used in this FSI routine is a discontinuous composite plate model based on Mindlin-Reissner Plate Theory, which was developed in previous work by the authors [19, 21]. In this model, the FishBAC is conceptualised as a series of partitioned plates connected together, with a new plate added at every chordwise and spanwise change in stiffness of the structure (e.g. when the spine has a stringer attached), to create a system of coupled analytical plate models. The Mindlin-Reissner plate formulation is used, and the differential equations are solved using the Rayleigh-Ritz Method. Furthermore, Classical Laminate Theory (CLT) is used to calculate the stiffness terms of the composite laminates [48]. This solution technique requires the use of assumed shape functions for the displacement, and in this application Chebyshev Polynomials of the First Kind have been selected. The coupling between adjacent plates is handled by first solving the plate equations for each partition, and then joining together the partitions using the Courant's penalty method in the form of artificial springs [49].

1. Rayleigh-Ritz Method

The Rayleigh-Ritz Method is a variational method that is used to approximate solutions to partial differential equations based on the principle of conservation of total energy in a closed system [48]. From a mechanics point of view, this implies that the sum of internal strain energy, potential energy due to internal loads and kinetic energy, is equal to zero (if friction is ignored). This total energy can be expressed in terms of the structure's displacements (u^0 , v^0 and w) and rotations (ψ_x and ψ_y), such that

$$\Pi(u^0, v^0, w, \psi_x, \psi_y) = U + V - T = \text{constant}, \quad (16)$$

where U , T and V are the strain, kinetic and potential energy due to external loads, respectively. As this model is for static load cases, the kinetic energy T is set to zero. The internal strain energy U can also be expressed as a function of structural displacement and rotations, as well as stiffness terms.

2. Strain Energy

For an elastic body, the strain energy is defined as the sum of the product of individual stress and strain components, integrated across the entire volume, as defined by the expression

$$U = \frac{1}{2} \iiint (\sigma_x \epsilon_x + \sigma_y \epsilon_y + \sigma_z \epsilon_z + \tau_{xz} \epsilon_{xz} + \tau_{yz} \epsilon_{yz} + \tau_{xy} \epsilon_{xy}) dx dy dz. \quad (17)$$

where σ and τ are the normal and shear stresses, respectively, and ϵ and γ are the normal and shear strains, respectively. In Mindlin-Reissner Plate Theory, through-thickness stress and strain are neglected, and therefore $\sigma_z = \epsilon_z = 0$ [48]. The remaining five strain can be expressed in terms of displacements and rotations—and their derivatives—as defined by the following equations:

$$\epsilon_x = \frac{\partial u^o}{\partial x} - z \frac{\partial^2 w}{\partial x^2}, \quad \epsilon_y = \frac{\partial v^o}{\partial y} - z \frac{\partial^2 w}{\partial y^2}, \quad \gamma_{xy} = \frac{\partial u^o}{\partial y} + \frac{\partial v^o}{\partial x} - 2z \frac{\partial^2 w}{\partial x \partial y} \quad \text{and} \quad (18)$$

$$\gamma_{xz} = \frac{\partial w}{\partial x} - \psi_x, \quad \gamma_{yz} = \frac{\partial w}{\partial y} - \psi_y. \quad (19)$$

The in-plane stresses can be expressed in terms of the *ABD* stiffness matrix—calculated using Classical Laminate Theory. The *ABD* Matrix describes the stiffness of the composite laminate; it combines both material and geometric stiffness in a single expression [50]. Moreover, the transverse shear stiffness terms are derived as

$$H_{ij} = \frac{1}{\kappa} \int_h \bar{Q}_{ij} dz = \frac{1}{\kappa} \sum_{k=1}^K \bar{Q}_{ij,k} (z_k - z_{k-1}) dz, \quad (20)$$

where $i, j = 4, 5$ and κ is known as the Timoshenko Shear Correction Factor, which has an approximate value of 6/5 for rectangular cross-sections. Although this approximation is valid for isotropic plates, results in the literature also show accurate predictions when used for composite plates [51]. Consequently, a constant value of $\kappa = 6/5$ is used in the FSI model. Lastly, \bar{Q}_{ij} refers to the local stiffness of each composite ply, and it is dependent on the fibre angle orientation. More details on how the final energy expressions are derived can be found in Rivero *et al.* [19, 21].

3. Shape Functions and Boundary Conditions

Since the plate's displacements and rotations are unknown—and are required to solve Eq. (18) when Eqs. (18)-(19) are substituted in—they need to be assumed in the form of shape functions. For two-dimensional structural models, these shape functions are normally assumed in the form of a double summation in both x and y directions. Therefore, the three displacements are defined as

$$u_{ij}^0 = \sum_{m=0}^M \sum_{n=0}^N L_{mn}^{ij} X_m^i(x) Y_n^j(y), \quad v_{ij}^0 = \sum_{m=0}^M \sum_{n=0}^N O_{mn}^{ij} X_m^i(x) Y_n^j(y) \quad \text{and} \quad w_{ij} = \sum_{m=0}^M \sum_{n=0}^N P_{mn}^{ij} X_m^i(x) Y_n^j(y), \quad (21)$$

and the transverse plane rotations have a similar formulation:

$$\psi_x = \sum_{m=0}^M \sum_{n=0}^N R_{mn}^{ij} X_m^i(x) Y_n^j(y) \quad \text{and} \quad \psi_y = \sum_{m=0}^M \sum_{n=0}^N S_{mn}^{ij} X_m^i(x) Y_n^j(y). \quad (22)$$

These shape functions (Eqs.(21)-(22)) have two main components: an unknown amplitude (i.e. L_{mn} , O_{mn} , P_{mn} , R_{mn} and S_{mn}) and the assumed shape functions $X_m(x)$ and $Y_n(y)$. The unknown amplitudes become the unknown variables of the system of equations, whereas the shape functions are prescribed as orthogonal polynomials. Specifically, Chebyshev Polynomials of the First Kind are selected as these prescribed shape functions, which are defined as

$$T(\zeta) = \frac{1}{2} \left[\left(\zeta - \sqrt{\zeta^2 - 1} \right)^n + \left(\zeta + \sqrt{\zeta^2 - 1} \right)^n \right], \quad (23)$$

where n corresponds to the polynomial order. To directly implement these polynomials, the physical plate's dimensions and coordinates need to be transformed to a normalized frame (i.e. $(\zeta, \eta) \mid (\zeta, \eta) \in [-1, 1]$) [19, 21].

Lastly, it is important to enforce the appropriate structural boundary conditions. The FishBAC is modeled as a cantilever plate clamped at its root, therefore, displacements and rotations must equal zero at this clamped edge. Since the Chebyshev Polynomials of the First Kind do not naturally meet this condition—as they have non-zero values at its boundaries—they need to be modified. To enforce boundary conditions, a circulation function [52]

$$\Gamma_x(\zeta) = (\zeta - \zeta_c)^n, \quad (24)$$

is added as a multiplier to all assumed displacements and rotations (i.e. Eqs. (21-22)). This circulation function enforces the shape function to have a certain value at the ζ_c location, and the nature of the boundary condition is defined by the value of n . Table 1 shows different boundary conditions and their corresponding n values [19].

4. Stiffness Discontinuities

Due to the presence of stringers and the chordwise taper (airfoil geometry), the FishBAC's stiffness is non-uniform along the chordwise direction. To account for these variations in stiffness, the structure is discretised in sections of uniform stiffness—using average dimensions—that are later joined together using a series of artificial penalty springs. These springs enforce displacement and rotation continuity at each 'joint'. The penalty terms are defined as

$$U_{pu,kl} = \frac{k_k}{2} \int_{-b_j/2}^{b_j/2} (u_k(x_{kl}^{(+)}, y_j) - u_l(x_{kl}^{(-)}, y_j))^2 dy, \quad (25)$$

where k and l refers to two adjacent plate partitions and the $+$ and $-$ signs represent the right and left hand sides of the discontinuity, respectively. One penalty function is required per each assumed displacement and rotation. Specifically, Eq. (25) represents the case where the discontinuity is along the chordwise direction. For spanwise discontinuities, equations of the same form apply but the integration is performed along the x -direction at $y_k^{(+)}$ and $y_l^{(-)}$ locations.

5. External Loads

In this Fluid-Structure Interaction analysis, there are two types of external loads acting on the structure: the aerodynamic pressure and the actuation torque inputs. The transverse pressure distribution is obtained by the aerodynamic solver (Section V.A) in terms of upper and bottom surface pressure distributions. A combined net aerodynamic pressure distribution is then assumed to be acting on the FishBAC's spine, and it is calculated by subtracting the top and bottom surface pressures

$$q_{\text{net}}(x, y) = (P_{\text{down}}(x, y) - P_{\text{up}}(x, y)) \quad (26)$$

Once the net pressure is obtained, it is incorporated to the structural model as potential energy due to external loads

$$V_{\text{pressure}}^{ij} = - \iint q(x, y) w(x, y) dx dy \quad (27)$$

Similarly, actuation loads are also incorporated as potential energy. In the FishBAC concept, the actuation loads are applied by a series of antagonistic tendons that transfer the loads from the servos to the structure using a pulley-tendon system. Consequently, these actuation loads are modeled as distributed moments at the location where the tendon and the composite plate meet. For distributed moments, the potential energy is equal to

$$V_{\text{actuation}}^{ij} = - \int M_x \psi_x(a_i, y) dy, \quad (28)$$

where a_i is the location where the distributed moment is applied. Note that this neglects any friction on the pulley-tendon system. The total potential energy due to external loads is equal to the sum of both V_{pressure}^{ij} and $V_{\text{actuation}}^{ij}$ [54].

Table 1 Boundary Conditions as implemented by circulation function in Eq. (24) [51, 53]

Boundary Condition at ζ_c	$n_{\text{displacement}}$	n_{rotation}	Disp. (u^o, v^o, w)	Rot. (ψ_x, ψ_y)	Transverse Shear Strains (γ_{xz}, γ_{yz})
Free Edge (F)	0	0	Free	Free	Free
Simply Supported (SS)	1	0	0	Free	Free
Clamped (C)	1	1	0	0	Free

6. Solution: System of Equations

As stated in Eq. (16), the principle of minimum potential energy is based on the assumption that the sum of all energy contributions is a constant value. Therefore, differentiating with respect to any of the unknown amplitudes (constants) L_{mn} , O_{mn} , P_{mn} , R_{mn} and S_{mn} results in a state of minimum potential energy—where the right hand side of Eq. (16) is equal to zero [55]. If the total energy formulation is differentiated with respect to each one of the unknown amplitudes, a system of $5 \times (M \times N) \times (i \times j)$ independent linear equations is generated as

$$\frac{\partial \Pi}{\partial L_{mn}^{ij}}, \frac{\partial \Pi}{\partial O_{mn}^{ij}}, \frac{\partial \Pi}{\partial P_{mn}^{ij}}, \frac{\partial \Pi}{\partial R_{mn}^{ij}}, \frac{\partial \Pi}{\partial S_{mn}^{ij}} = 0 \quad \begin{cases} m = 1, 2, \dots, M \\ n = 1, 2, \dots, N \end{cases} \quad (29)$$

Once all the unknown constants are obtained through solving this systems of equations, all displacements (Eq. (21)) and rotations (Eq. (22)) fields can be constructed. This analytical model represents a fast, parametrically driven, robust approach to modeling the behavior of the FishBAC morphing device[19].

7. Model Validation

The discontinuous plate-based Mindlin-Reissner model was validated against FEM by Rivero *et al.* (2019) [19]. This validation was performed by tracking spanwise displacements along the FishBAC spine's three free edges, and then comparing both plate model and FEM results. Average and maximum percentage differences of 6.2% and 9.1%, respectively, were reported. Considering that the plate-based model has only 1% of the DOFs compared to FEM, it was considered that this worst-case percentage difference was acceptable for design and optimization purposes.

C. FSI Analysis Numerical Implementation

The 3D composite FishBAC FSI routine 'loosely' couples the structural and aerodynamic solvers. In this case, the aerodynamic solver runs ahead of the structural solver, hence, the aerodynamic solution in the first iteration corresponds to a rigid NACA 23012 wing with no deformations. These initial aerodynamic results are used as input by the structural solver along with the actuation input settings, leading to an initial FishBAC displacement field that is then used to generate a deformed set of airfoil geometries in the second iteration.

1. Airfoil Geometry Generator

The FishBAC's airfoil profile has two different sections: the main rigid section (i.e. $0 < x/c < 0.744$)—maintained rigid throughout the analysis—and the morphing portion (i.e. $0.744 < x/c < 1$). The main rigid section's airfoil profile is obtained from the NACA 5-digit equations [47], using the NACA 23012 input parameters. As the FishBAC's structural solver models the spine's displacement, the airfoil geometry needs to be constructed from the spine's transverse displacement field. To achieve this, a sixth-order polynomial fit is performed to capture the local spine deformation at a given spanwise location. A high-order polynomial fit ensures that complex spine deflections can be captured [56]. The airfoil shape is rebuilt on top of the current deflected spine shape by applying the airfoil's thickness distribution at each point along the length of the spine normal to the local tangent of the spine. This process is identical to the NACA method of defining airfoils, and also reflects the role of the stringers in maintaining the thickness distribution with camber change. This airfoil reconstruction process is performed at each spanwise LLT control point (see Section V.A.1).

2. Coupling Algorithm

Once the airfoil geometries have been generated, the aerodynamic solver obtains converged pressure distributions and aerodynamic coefficients at each Lifting-Line control point. To ensure matching coordinates between the structural and the aerodynamic models, the structural model's spanwise partitions are assigned so that each partition boundaries are aligned with the local horseshoe element. The pressure distribution at each control point is then applied to the structural model along with the external actuation input moments. The FSI analysis outputs a converged FishBAC's displacement field, followed by a convergence check on the total lift coefficient. The FSI routine is said to be converged when the change in lift coefficient between two subsequent iterations is less than 0.5%

$$C_{L_{err}} = \frac{|C_L(k) - C_L(k-1)|}{C_L(k-1)} \leq 0.005, \quad (30)$$

where k refers to the FSI iteration counter. Fig. 6 shows a schematic of the implemented coupling algorithm.

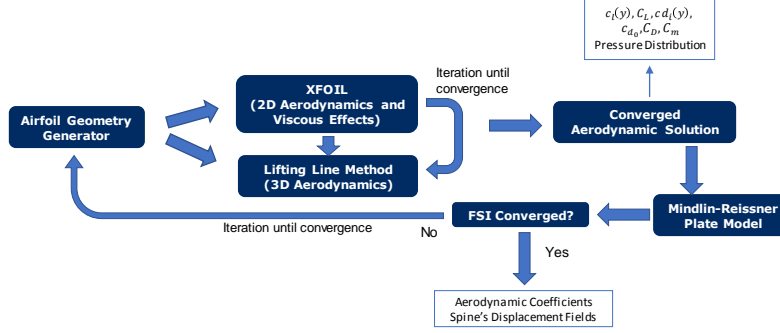


Fig. 6 Schematic of the loosely-coupled fluid-structure interaction (FSI) routine

3. Relaxation Factors

Relaxation factors are used in numerical methods to stabilize solutions that are obtained via iterative methods, hence, assisting convergence. They reduce the step size between two expected solutions, reducing the likelihood of undesired fluctuations that may lead to divergence. Consequently, it can be said that relaxation factors add ‘damping’ to the numerical solution [56–58]. In fluid-structure interaction algorithms, relaxation factors are normally applied between the structure and aerodynamic interface. For this FishBAC FSI analysis, fixed relaxation parameters are applied to both structural and aerodynamic solutions. For the structural solution, relaxation is applied to the spine displacement field

$$w_{\text{new}}^r(x, y) = \frac{w_{\text{new}}(x, y)\lambda_w + w_{\text{old}}(x, y)}{\lambda_w + 1} \quad (31)$$

where λ_w refers to the relaxation factor on the spine displacement. Similarly, relaxation is applied to the net aerodynamic pressure obtained from the aerodynamic solver

$$q_i^r(x, y) = \frac{q_i(x, y)\lambda_p + q_{i-1}(x, y)}{\lambda_p + 1} \quad (32)$$

where λ_p is the relaxation factor for pressure distribution. Increasing the value of the relaxation values λ_w and λ_p would lead to a slow but stable solution, whereas a value of zero corresponds to no relaxation. Although widely used in numerical methods, it is important to note that the selection of these relaxation values is highly empirical, and hence, they must be ‘tuned’ for each application [59]. For this FSI model, a value of λ_w and λ_p between 0.1 and 0.5 was found to be sufficient for convergence.

4. Model Implementation

The FSI model is implemented in MATLAB using an open-source wrapper that executes XFOIL. The remaining structural and aerodynamic calculations are all solved using MATLAB’s built-in functions. The geometric dimensions of the wing model are 270 mm in chord and 2000 mm in span, resulting in an aspect ratio of $AR = 7.4$. A NACA 23012 airfoil was selected as the baseline profile, and the morphing FishBAC portion of that airfoil starts at $x/c = 0.744$. The remaining non-morphing section of the wing is assumed to be rigid, hence, it does not deform during the FSI analysis. Lastly, a taper ratio of 1 (untapered) and a dihedral angle $\phi = 0$ were used for this analysis.

Regarding the structural model, three different material properties are used to model the morphing section: 8552/IM7 carbon fiber-reinforced prepreg (spine), 3D printed ABS plastic (stringers) and silicone rubber sheet (skin). These materials properties were obtained by performing a series of material characterization experiments, which are thoroughly discussed in Rivero *et al.* [18]. Also, five Chebyshev polynomial terms were used, whereas the penalty spring stiffness of all penalty terms was set to $k = 1 \cdot 10^7 \text{ N m}^{-1}$. More specific details on how the structural model is implemented—including internal dimensions and assumptions—can be found in previous publications [19, 21].

Finally, four aerodynamic input parameters are needed to execute the FSI model: freestream velocity, air density, angle of attack and Reynolds number. In this study, the freestream velocity was set to $V = 30 \text{ m s}^{-1}$, which corresponds to a Mach number of $M = 0.089$ at standard sea level (SLS) conditions. Additionally, the air density at SLS conditions is equal to $\rho_\infty = 1.225 \text{ kg m}^{-3}$, resulting in a Reynolds number of $Re \approx 543000$. Lastly, an angle of attack sweep from $\alpha = -4^\circ$ to $\alpha = 14^\circ$, in increments of 2° , was performed for each test case.

A total of 107 actuation input combinations were run in this analysis, including uniform actuation inputs at both actuators, single actuation (i.e. only one actuator being used) and different permutations of positive and negative torque inputs.

VI. Model Validation

The aerodynamic model was validated against a similar nonlinear LLT model developed by Tornero [60] as well as the XFLR5 open-source code. XFLR5 is a 3D wing analysis software capable of analyzing the aerodynamics of finite wings using either Lifting-Line Theory, Vortex Lattice Method or 3D Panel Method. Additionally, it corrects for viscous effects by interpolating XFOIL results at local airfoil sections. For the LLT case, the viscous analysis is fully coupled, and it iterates both 2D viscous and 3D solutions until convergence is met. For the VLM and 3D panel case, a viscous correction is implemented to the final drag value. Therefore, the viscous LLT option is used for validation as it more fully includes viscous effects, as long as the code is used within LLT's limitations [61].

It is important to note that XFLR5's drag calculations differ from traditional LLT ones as it calculates it using far-field methods—i.e. at the Trefftz Plane. Far-field methods are based on conservation of momentum downstream of the body, whereas LLT calculates drag at the near-field—i.e. at the wing's surface [61]. Even though drag calculations at the near-field tend to be higher than at the far-field, near-field estimates tend to be very robust as they only depend on the local flow properties at the wing surface. In contrast, Trefftz-plane drag calculations tend to be more accurate, but may yield to incorrect results if calculation are performed inside the wake [62]. In summary, XFLR5 drag estimates are expected to be lower than those obtained by the implemented aerodynamic model, which calculates drag at the near-field.

Additionally, to ensure consistent and accurate results, a convergence study on how lift coefficient is affected by varying the number of spanwise horseshoe elements was performed. To evaluate this, the angle of attack was set to $\alpha = 5^\circ$ (to ensure fully attached flow) and an actuation input of $M_x = -2 \text{ N m}$ was applied at each actuation point. Under these conditions, a maximum FishBAC deflection of $x/c \approx 9\%$ is achieved. Lastly, the spanwise panel number was varied from 20 to 120, in increments of 10. The model is said to be converged when the change in 3D lift coefficient with increasing number of spanwise elements is less than 0.1%. Based on this convergence study, a total of 60 spanwise elements are used.

Lastly, to validate the fluid-structure coupling algorithm, a 2D comparison was performed against Woods and Friswell's XFOIL/Euler-Bernoulli FSI model [33]. To establish this comparison, the composite spine stiffness was 'homogenised' to obtain an equivalent Young's modulus [63] that can be used in Woods and Friswell's beam model. Furthermore, to simulate a 2D flow condition, downwash was suppressed on the 3D FSI model and the span was set to 25 mm—which corresponds to the width of one of the actuation tendons.

VII. Results

This section presents the FSI model results. The section is divided into two subsections: model validation and camber morphing wing performance studies.

A. Model Validation

The validation of the FSI routine involves three different different aspects: aerodynamic model, structural model and FSI routine validations. Since the structural model was validated in a previous study (see Section V.B.7), this section focuses on the aerodynamic model and FSI validations.

1. Aerodynamic Model

To validate the nonlinear Lifting-Line Theory model, a rigid NACA 23012 wing was analyzed using a nonlinear LLT routine developed by Tornero [60], as well as XFLR5's nonlinear LLT routine (Fig. 7) [61]. Percentage differences in lift and drag coefficients between the current model and Tornero's and XFLR5 models were calculated. Results show good agreement between Tornero's model and the FSI's aerodynamic model, with an average percentage difference of 0.658% and 1.001% in lift and drag, respectively. Furthermore, the percentage difference with respect to XFLR5's LLT's model becomes 8.42% and 8.62% in lift and drag, respectively. It is important to note that, when looking at single values of drag coefficients, there is a direct correlation between increasing angle of attack and increasing percentage difference—with the LLT's FSI model presenting higher drag values.

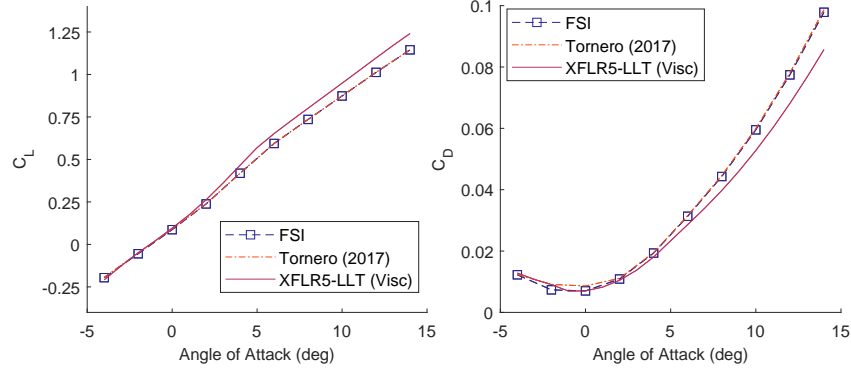


Fig. 7 Aerodynamic model validation: lift and drag coefficient comparison

This discrepancy is potentially due to XFLR5's drag calculations being performed at the Trefftz plane, whereas both Tornero's and the FishBAC nonlinear LLT model calculate drag at the near-plane. As described by XFLR5's user guide, drag calculations at the near-field tend to be higher, especially at high angles of attack [61].

In summary, the FSI nonlinear LLT model accurately predicts lift coefficient when compared to two other LLT-based solvers. However, discrepancies in drag exists, especially at high angles of attack. These discrepancies are likely due to slight differences in modeling techniques between traditional nonlinear LLT and XFLR5's nonlinear LLT. Therefore, it is important to treat drag estimates at high angles of attack with care, especially when it is well known that Lifting-Line theory may become inaccurate in modeling separated flows.

2. FSI Validation

The FSI model validation was performed in two steps: (i) a 2D comparison to Woods and Friswell's 2D FSI [33] and (ii) a 3D aerodynamic validation of the converged deformed shapes using XFLR5's.

(i) 2D Validation

The 3D FishBAC FSI model was directly compared to a previously developed 2D FishBAC FSI [33]. Fig. 8 shows a comparison of lift and drag coefficients obtained by using each modeling technique. The lift and drag coefficient results show a good agreement between 2D FSI (beam model + XFOIL) and 3D FSI (plate model + LLT) routines. Percentage differences in lift coefficients of less than 3% are observed for all five actuation cases. Additionally, the deformed shapes were also compared. Fig. ?? shows the converged spine deflections as a function of torque input. An average discrepancy of less than 5% is observed between the two modeling techniques. In summary, the two models agree with each other, which confirms that the coupling routine of the 3D composite FishBAC FSI works accordingly.

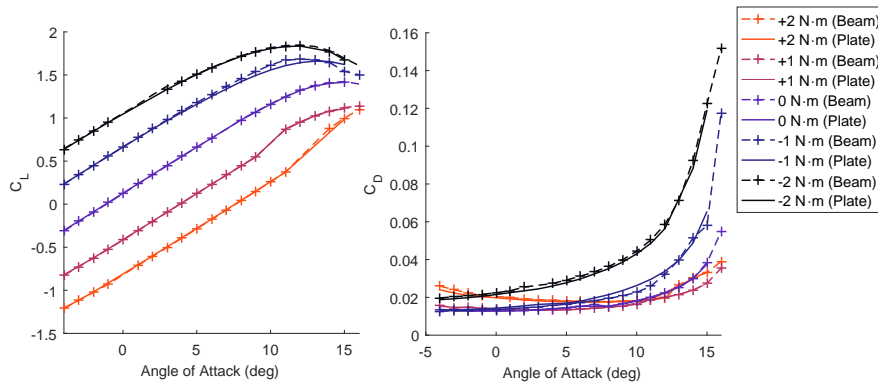


Fig. 8 2D FSI validation—lift and drag coefficients as a function of angle of attack

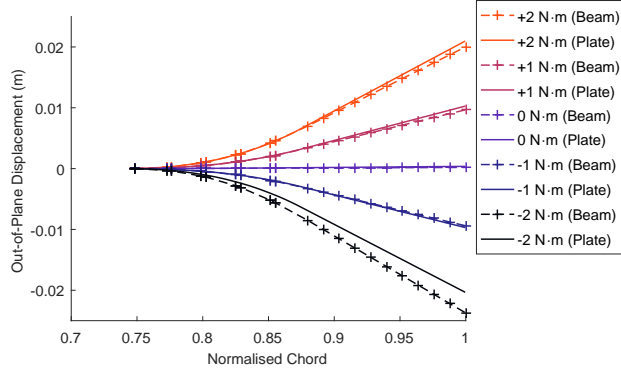


Fig. 9 2D FSI validation—FishBAC spine deflection

(ii) 3D Comparison

The final step of the validation process is to compare the aerodynamic behavior of several FSI converged deformed shapes. To perform this comparison, three different load cases were considered at several angles of attack: (i) $M = -1$ N m uniform actuator input at both actuators, inducing a large downward FishBAC deflection (ii) $M = 0.25$ N m uniform actuator input, resulting on a small upward FishBAC deflection and (iii) a single actuation input of $M = -0.75$ N m at the outboard actuation only, inducing significant spanwise variations in transverse displacements.

These deformed airfoil shapes were extracted from the FSI solver and then input into XFLR5—where the nonlinear viscous LLT analysis was performed. Five different angles of attack were considered: two negative ($\alpha = -4^\circ, -2^\circ$), zero ($\alpha = 0^\circ$), low positive ($\alpha = +5^\circ$) and a high positive angle of attack ($\alpha = +12^\circ$). Fig. 10 shows the uniform negative actuation case as example. Moreover, percentage differences in lift and drag coefficients were calculated and results are summarised in Table 2.

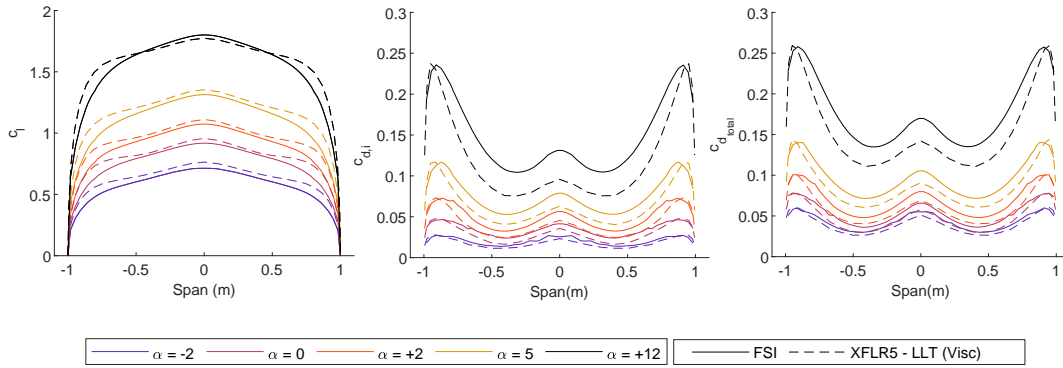


Fig. 10 Aerodynamic Comparison between FSI converged aerodynamics and XFLR5's LLT, for an actuation input of $[M_{x_1}, M_{x_2}] = [-1, -1]$ N m

Table 2 FSI validation test cases in terms of percentage difference in lift and drag coefficients (NC = not converged)

Load Case [M_{x1}, M_{x2}]	α (deg)	ΔC_L (%)	ΔC_D (%)
[-1, -1] N m	-2	8.55	9.49
	0	6.34	12.62
	2	5.89	14.55
	5	6.14	13.31
	12	2.90	8.78
[+0.25, +0.25] N m	-2	NC	NC
	0	NC	NC
	2	NC	NC
	5	9.58	4.77
	12	6.19	8.90
[0, -0.75] N m	-2	13.27	1.010
	0	10.135	3.90
	2	8.679	4.915
	5	8.294	8.128
	12	NC	NC
Average		7.82	8.81

It is observed in Table 2 that an average percentage difference in lift and drag coefficients of 7.82% and 8.81%, respectively, exists. Moreover, it is observed that these values are highly dependent on the load case and angle of attack. For example, the lift coefficient percentage difference ranges between 2.90% to 13.27%, whereas the drag coefficient varies between 1.01% and 14.55%. Also, Fig. 10 shows that trends in spanwise lift and drag distributions are well captured. Discrepancies in results could be due to either slight differences in calculating aerodynamic forces—as explained in the previous subsection—or due to discrepancies in the 2D airfoil data used for viscous corrections. As previously mentioned, the 2D airfoil data is obtained by running XFOIL using the local airfoil geometry at each horseshoe element, for a wide range of angles of attack. XFOIL sporadically fails to converge at certain airfoil geometries and angles of attack, and therefore, the effective angle of attack interpolations may be affected due to the lack of certain data points. One important observation from these results is that the highest percentage difference in drag values occur at the highest camber deflection—when both actuation inputs were $M_x = -1$ N m. Consequently, it was decided to reduce the maximum torque input per actuator to $M_x = -0.75$ N m. In summary, for the majority of cases, the FSI aerodynamic results agree with XFLR5’s estimates with a percentage difference of less than 9%. However, these differences may increase up to 13% for certain cases, especially when larger camber deflections occur.

B. Aerodynamic Coefficients

This subsection introduces how the three main aerodynamic coefficients— C_L , C_D and C_m —vary with increasing FishBAC deflection. The first case to be considered is symmetric load input, where both actuators in each half-wing apply the same amount of torque.

1. Case 1: Symmetric Actuation

Fig. 11 shows the lift, drag and moment coefficients as a function of angle of attack and symmetric actuation inputs. Results show that the FishBAC presents a lift control authority of $\Delta C_L \approx 0.5$ when downward FishBAC deflections are considered. As expected, increasing deflection also increases drag, resulting in a change of drag coefficient that ranges from $\Delta C_D \approx 0.02$ to $\Delta C_D \approx 0.08$, for angles of attack between $\alpha = 0^\circ$ and $\alpha = +14^\circ$. Furthermore, a change in pitching moment coefficient between $\Delta C_m \approx 0.1$ and $\Delta C_m \approx 0.14$ is achieved when downward FishBAC deflections are considered. Although these results highlight the FishBAC’s control authority, they do not provide sufficient information to assess aerodynamic efficiency. Therefore, lift-to-drag ratios as a function of angle of attack and lift coefficient are presented in Fig. 12.

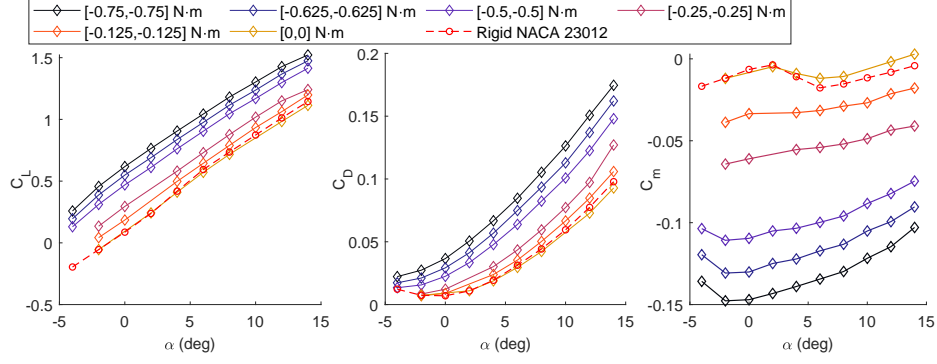


Fig. 11 Lift, drag and moment coefficient as a function of angle of attack and actuation inputs. Actuation inputs are symmetric

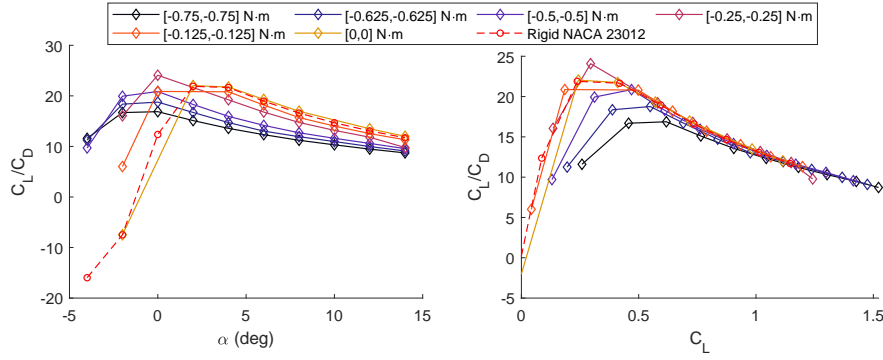


Fig. 12 Aerodynamic efficiency as a function of angle of attack and lift coefficient. Actuation inputs are symmetric

It is observed in Fig. 12 that a higher aerodynamic efficiency than the rigid NACA 23012 airfoils can be achieved at low angles of attack and low lift coefficients. However, these efficiency gains decrease as lift coefficient increases. Since the majority of the drag at high lift coefficients comes from the induced drag due to lift, having higher camber deflections at the wing root and gradually reducing them towards the wingtip may be beneficial for reducing induced drag. Therefore, if the actuation inputs are applied such that the wing tips are ‘offloaded’, higher aerodynamic efficiencies may be achieved. To assess the potential of these asymmetric deflections, a load case where only one actuator applies torque is considered in Section VII.B.2.

2. Case 2: Single Actuation Input

One way to estimate whether higher aerodynamic efficiency can be achieved by asymmetric actuation is to compare how aerodynamic coefficients vary if only one actuator is used in each half-wing. To determine the effect of using the inboard versus the outboard actuators, torque magnitude is kept constant and the actuation location is changed from inboard to outboard actuators. Fig. 13 shows the lift, drag and moment coefficients for two pairs of actuation inputs: -0.75 N m and -0.625 N m at both inboard and outboard actuators, respectively. Results show that there is no significant change in lift coefficient with varying actuation location, however, a drag coefficient reduction between 2% and 5% is observed when the inboard actuator is used. In general, using the inboard actuator yields lower drag coefficients for all angles of attack. When compared in terms of aerodynamic efficiency as a function of both angle of attack and lift coefficient (Fig. 14), it is observed that an increase in efficiency over the baseline rigid airfoil of between 10% and 50% is achieved at low lift coefficients (i.e. $C_L < 0.5$), whereas an increase between 3.5% and 6.75% is observed for higher lift coefficients. These results are consistent with the fact that generating less lift near the wingtips would lead to a reduction in downwash at the wingtips—where it normally has its highest value in finite wings. Therefore, offloading the tips leads to lower induced drag and, thus, higher efficiency. However, using only one actuator comes at the expense of achieving lower lift coefficients due to lower camber deflections. Therefore, an alternative to obtain higher lift and lower

drag coefficients, respectively, is to apply different non-zero actuation inputs at both inboard and outboard actuators.

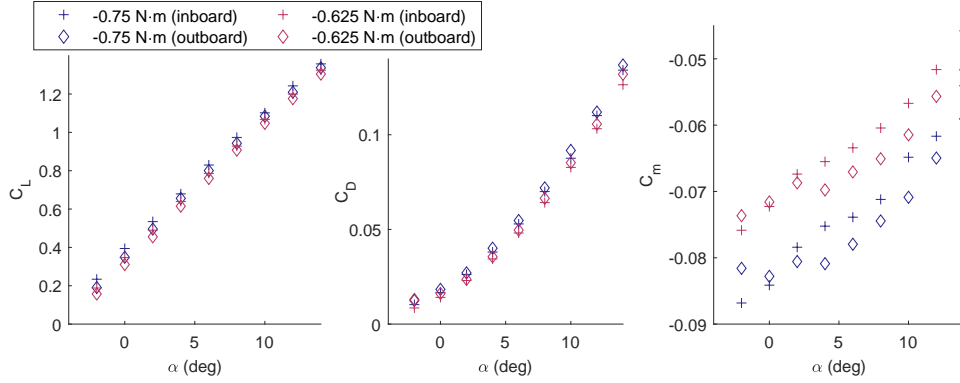


Fig. 13 Lift, drag and moment coefficient as a function of angle of attack when only one actuator is used

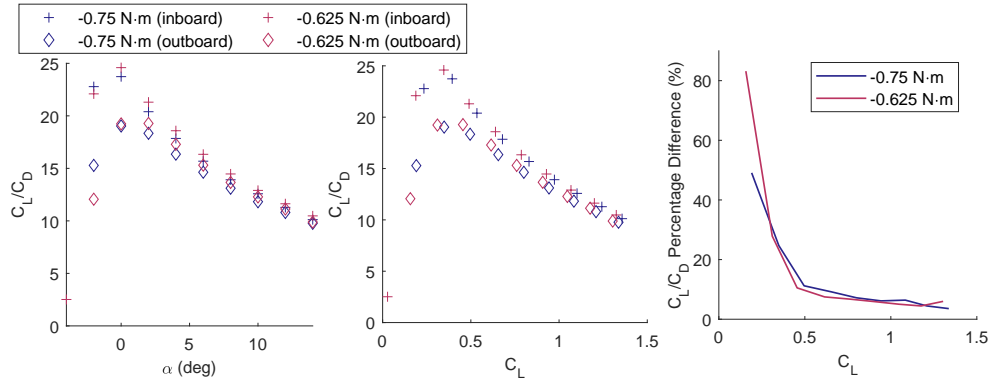


Fig. 14 Aerodynamic efficiency as a function of angle of attack and lift coefficient when only one actuator is used

3. Case 3: Asymmetric Actuation Inputs

The third actuation case to be considered is when asymmetric actuation inputs are used—i.e. when the torque inputs at each inboard and outboard actuators are not equal. To fully explore the ‘control space’, a total of 117 configurations were studied, with torque values ranging from -0.75 N m to 0.25 N m and for angles of attack between $\alpha = -4^\circ$ and $\alpha = +14^\circ$, in increments of $\alpha = 2^\circ$. One way of analyzing the resulting aerodynamic properties is to estimate the lift (Fig. 15) and drag (Fig. 16) coefficients, respectively, as a function of torque inputs and angle of attack. Each of the colored surfaces in Fig. 15 represent the FishBAC’s lift control authority at a given angle of attack when all combinations of positive and negative actuation inputs are considered. An average lift control authority of $\Delta C_L = 0.58$ is achieved across all angles of attack, having a maximum value of $\Delta C_L = 0.63$ at $\alpha = 6^\circ$ and a minimum value at $\Delta C_L = 0.50$ at $\alpha = 14^\circ$. Also, an average change in drag coefficient of $\Delta C_D = 0.066$ is observed in Fig. 16. These results show that a wide range of lift coefficients can be achieved without varying angle of attack. Also, results suggest that the additional drag due to these camber deflections is at least one order of magnitude lower than the increase in lift.

When observed in terms of lift-to-drag ratio (Fig. 17), it is seen that C_L/C_D can widely vary with torque input. Hence, it may be difficult to estimate which one is the best actuation input and angle of attack that yields to the best aerodynamic efficiency. Since angle of attack and torque inputs can be controlled and set to a desired value—within torque available limits—one alternative to evaluate the aerodynamic performance is to calculate the maximum achievable lift-to-drag ratio across the range of achievable lift coefficients. By doing so, the aerodynamic performance can be analyzed in terms of a condensed metric that inherently considers all possible combinations of actuation inputs, angles of attack and camber deflections.

This condensed metric is particularly useful when comparing the aerodynamic performance of different trailing edge devices (e.g. FishBAC vs flap), as it can establish a direct comparison between different configurations that is independent of variables that may be different depending on the device—e.g. actuation inputs, camber deflections, angles of attack and flap angles.

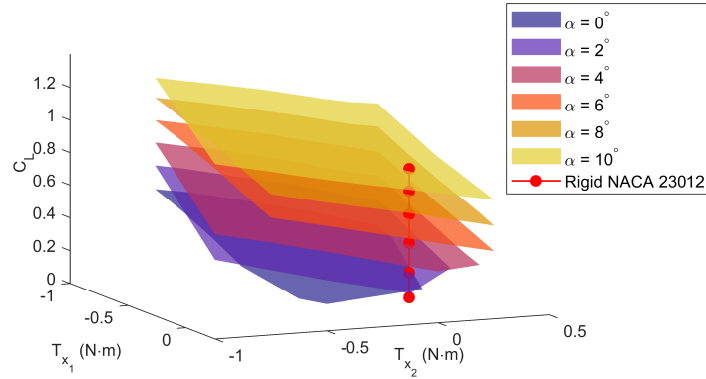


Fig. 15 Lift coefficient as a function of angle of attack and actuation torque inputs

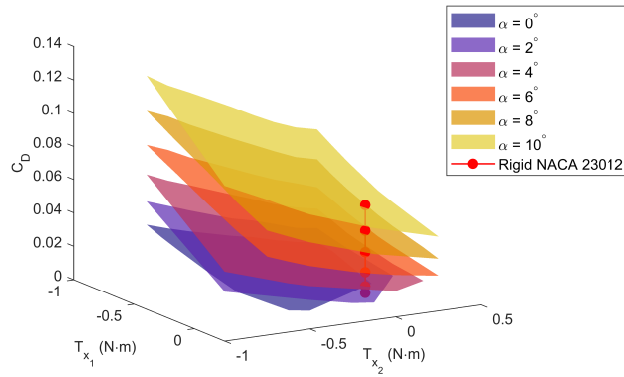


Fig. 16 Drag coefficient as a function of angle of attack and actuation torque inputs

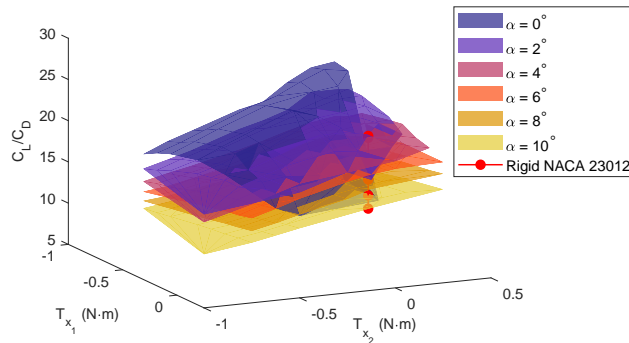


Fig. 17 Lift-to-drag ratio as a function of angle of attack and actuation torque inputs

Consequently, the aerodynamic efficiency (lift-to-drag ratio) of the FishBAC wing is now analyzed as a function of achievable lift coefficients. Fig. 18 shows all the lift-to-drag ratios corresponding to the different angles of attack and actuation combinations that were considered. In this figure, the left-hand side plot (Fig. 18a) represents all the achieved lift-to-drag ratios for each angle of attack, whereas the right-hand side plot (Fig. 18b) represents the best aerodynamic efficiency that can be achieved at each angle of attack, as a function of lift coefficient.

Moreover, angle of attack can be removed from this comparison by selecting the best aerodynamic efficiency that can be achieved at a given lift coefficient. By doing so, a direct comparison between FishBAC's and other configurations' best performances can be established. To directly compare the FishBAC to a traditional control surface, a plain flap of equal percentage chord was evaluated using the built-in flap functionality of XFOIL and the same 3D aerodynamic nonlinear LLT. These flapped airfoils are likely to have lower than reality drag values due to the lack of a gap between the flap the rest of the wing and due to the lack of control horns, but they provide a useful initial comparison. Flap deflections of between $\delta = -30^\circ$ and $\delta = +20^\circ$, in increments of $+10^\circ$, were evaluated at the same operating condition as the rigid and FishBAC wings. Results show that the FishBAC has an aerodynamic efficiency improvement over the flap of at least 44% for lift coefficients between $C_L = 0.08$ and $C_L = 0.42$ (Fig. 19). However, these efficiency improvements reduce to 5% for lift coefficients greater than $C_L = 0.42$. Although the FishBAC is more efficient than the flap at all lift coefficients, there is a clear reduction in efficiency gains as lift coefficient increases. These results suggest that this is potentially due to a rapid increase in induced drag as lift increases.

To further investigate the increase in induced drag with increasing lift, the corresponding total, induced and profile drag coefficients for the best performing examples (as a function of lift coefficient) of each configuration are compared. Fig. 20 shows these results, plotted on a double y-scale with the induced drag's contribution to the total drag coefficient shown as a percentage. These results consistently show that profile drag dominates for lift coefficients lower than $C_L \approx 0.38$. At lift coefficients above $C_L \approx 0.4$, induced drag rapidly grows, and it represents approximately 85% of the total drag for lift coefficients above $C_L > 1.3$ in both FishBAC and flap configurations. These results explain why the aerodynamic efficiency improvements of the FishBAC diminish at higher lift coefficients. Therefore, it can be concluded that for the wing design investigated here, the benefit of using the FishBAC is more significant when profile drag is higher than induced drag.

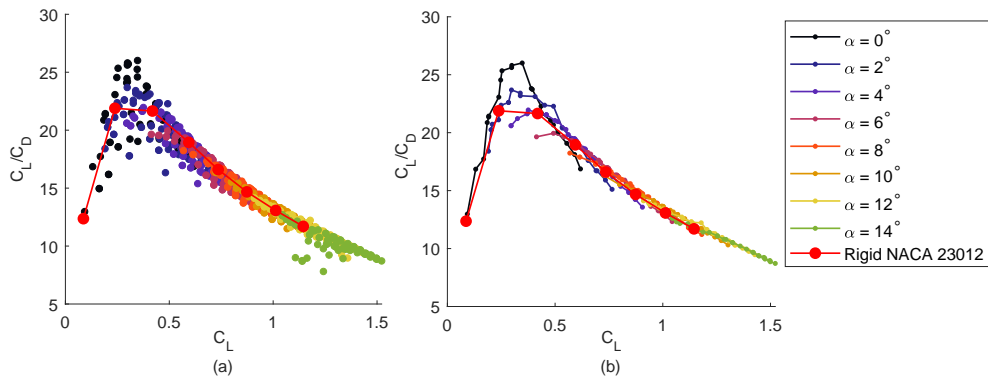


Fig. 18 Lift-to-drag ratio as a function of angle of attack and actuation torque inputs

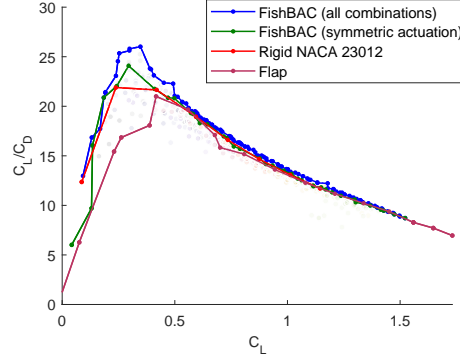


Fig. 19 Lift-to-drag ratio as a function a of angle of attack and actuation torque inputs

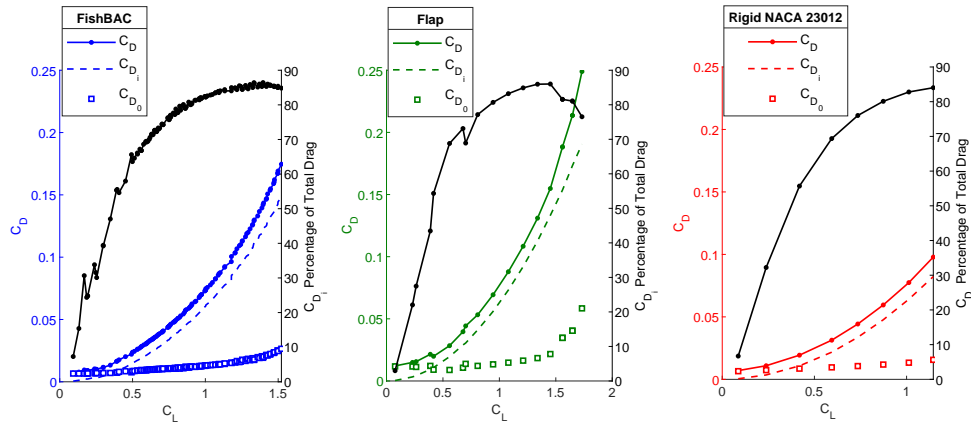


Fig. 20 Comparison between total, induced and profile drag coefficients

4. Case Study: Constant Lift Coefficient

Airplanes spend the majority of a flight at cruise condition. These cruise operations normally occur at wings-level equilibrium flight—i.e. when lift equals weight and no vertical acceleration occurs. However, as the weight of the aircraft decreases due to fuel burn, the required lift to maintain equilibrium flight also decreases. To maintain equilibrium, one way of reducing the lift force that is generated is to change angle of attack. However, there will be a drag penalty due to an increase in fuselage drag if angle of attack is decreased. An alternative is to ‘trim’ the aircraft by actively using control surfaces, also resulting in a drag penalty (trim drag) that is usually lower than the increase in drag due to change in angle of attack [64]. A third option is to decrease lift by increasing altitude, which reduces the aerodynamic forces due to a reduction in air density. Although effective, these changes in altitude may be limited by the aircraft service ceiling and other operational constraints. The adaptability of a morphing wing could allow to efficiently vary the amount of lift without varying angle of attack and/or altitude, without the associated drag penalty of hinged control surfaces.

To further study this hypothesis, the best achievable drag coefficients at constant lift coefficients and angles of attack have been interpolated from the FishBAC data set using a triangulation linear interpolation function. Fig. 21 shows the resulting drag coefficients as a function of constant lift coefficients and angles of attack.

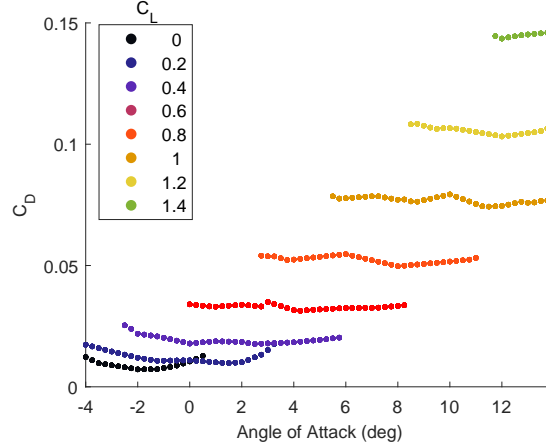


Fig. 21 Drag coefficients as a function of fixed lift coefficients and angle of attack

There are two main points that can be inferred from these results: (i) a change in lift coefficient of at least $\Delta C_L = 0.4$ (and often up to $\Delta C_L = 0.8$) can be achieved at each angle of attack and (ii) the minimum achievable drag associated with each lift coefficient is relatively constant and independent of angle of attack. In other words, a significant change in lift coefficient can be achieved without changing angle of attack. This ability to change lift coefficient at a constant angle of attack may be desirable in certain manoeuvres, as lower drag values could be achieved by maintaining the fuselage levelled with respect to the horizontal plane. Also, Fig. 21 shows that certain lift coefficients can be achieved at a wide range of angles of attack without significant drag increases. These results highlight how adaptive a FishBAC morphing wing is and how this can be exploited for improving aerodynamic efficiency at a broad range of angles of attacks and lift coefficients.

Finally, these resulting constant lift coefficients can be observed as a function of their corresponding drag coefficients as seen in Fig. 22. Given this range of obtainable results, the non-dominated points across the entire data set can be determined to create the Pareto frontier of each set [65]. This Pareto frontier represents the lift coefficients that can be achieved at the lowest drag penalty, thus maximizing lift-to-drag ratio for a desired C_L . Also, Fig. 22 shows the converged flap results and its corresponding Pareto frontier. As observed, the FishBAC presents lower drag coefficients for all lift coefficients and the area between the two Pareto frontiers represents the aerodynamic efficiency gains.

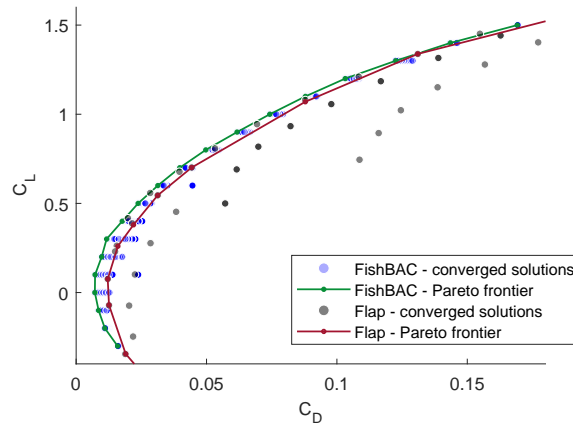


Fig. 22 Pareto frontier of achievable lift coefficients as a function of drag coefficients for both FishBAC and flap

VIII. Conclusions

This paper introduces a 3-dimensional Fluid-Structure Interaction analysis of a composite FishBAC camber morphing wing. The loosely-coupled routine is based on a discontinuous Mindlin-Reissner plate model and a viscous corrected nonlinear Lifting-Line Model for the structural and aerodynamic solvers, respectively. This model is capable of obtaining converged three-dimensional lift, drag and moment coefficients and aerodynamic pressure distributions, for a prescribed Mach number, angle of attack, actuation torque inputs and Reynolds number. After performing an analysis at a Mach number of $M = 0.089$ and a Reynolds number of $Re \approx 543,000$ on a simple rectangular planform wing test case, the following conclusions were drawn:

- 1) The 3D composite FishBAC device has a lift control authority of between $\Delta C_L = 0.5$ and $\Delta C_L = 0.63$, for the actuation inputs considered
- 2) Actuation inputs that lead to lower camber deflections in the outboard section of the wing lead to a higher overall aerodynamic efficiency. Offloading the tip has a direct impact on reducing induced drag. An increase in lift-to-drag ratio between 5% and 7% can be achieved by this induced drag reduction.
- 3) The FishBAC wing is capable of achieving a wide range of constant lift coefficients across a wide range of angles of attack by varying actuation input. At these constant lift coefficient cases, the drag coefficient remains relatively stable when varying angle of attack. This feature highlights how adaptive the FishBAC morphing wing can be for a wide range of angles of attack and lift coefficients
- 4) The FishBAC presents a 44% higher aerodynamic efficiency than a plain flap wing, for low lift coefficients between $C_L = 0.08$ and $C_L = 0.42$. However, this percentage improvement decreases to 5% when lift coefficients above $C_L = 0.42$ are considered. This performance decrease at high angles of attack is due to induced drag becoming significantly larger than profile drag at higher lift coefficients—an effect exacerbated by the rectangular, untwisted planform considered here as an initial test case.
- 5) In terms of components of total drag, profile drag dominates for lift coefficients below $C_L = 0.38$. For lift coefficients above this value, induced drag rapidly grows, and becomes $> 85\%$ of the total drag for lift coefficients greater than $C_L > 1.3$. Therefore, introducing design features to reduce induced drag (e.g. twist, taper, and higher aspect ratio) could potentially lead to further enhanced FishBAC behavior for more sophisticated wing designs operating at higher lift coefficients.

Future Work

Future work will consider different wing planform configurations where features to reduced drag are introduced. For example, introducing twist and taper or increasing aspect ratio may lead to higher FishBAC performance at high angles of attack, when compared to a plain flap. Also, future work will focus on applying similar modeling techniques to evaluate the FishBAC's behavior at higher Mach and Reynolds numbers, respectively—a critical step towards full-scale applications in fixed-wing aircraft.

Acknowledgments

This work was supported by the Engineering and Physical Sciences Research Council through the EPSRC Centre for Doctoral Training in Advanced Composites for Innovation and Science [grant number EP/L016028/1].

Furthermore, this project has received funding from the European Union's Horizon 2020 research and innovation programme under grant agreement No. 723491 as part of SABRE: Shape Adaptive Blades for Rotorcraft Efficiency.

Data Access Statement

All underlying data are provided in full within this paper.

References

- [1] Henry, A. C., "Performance Augmentation of Compliance-Based Morphing Wings Through Optimization and Nonlinearity," Ph.D. thesis, Purdue University, 2017.
- [2] Greff, E., "The development and design integration of a variable camber wing for long/medium range aircraft," *The Aeronautical Journal*, Vol. 94, No. 939, 1990, pp. 301–312.
- [3] Recksiek, M., "Advanced High Lift System Architecture With Distributed Electrical Flap Actuation," *2nd International*

- Workshop on Aircraft System Technologies*, Hamburg, Germany, 2009, pp. 1–11.
- [4] Parker, H., “The Parker Variable Camber,” Tech. Rep. 77, National Advisory Committee for Aeronautics, Washington, DC, 1920.
 - [5] Hogan, H. J., “Variable Camber Airfoil,” *U.S. Patent 1,868,748*, 1932.
 - [6] Chilton, R., “Variable Area-and-Camber Wing,” *U.S. Patent 2,222,935*, 1940.
 - [7] Barbarino, S., Bilgen, O., Ajaj, R. M., Friswell, M. I., and Inman, D. J., “A Review of Morphing Aircraft,” *Journal of Intelligent Material Systems and Structures*, Vol. 22, No. 9, 2011, pp. 823–877. doi:10.1177/1045389X11414084.
 - [8] Bilgen, O., Friswell, M. I., Kochersberger, K. B., and Inman, D. J., “Surface Actuated Variable-Camber and Variable-Twist Morphing Wings Using Piezocomposites,” *Structures, Structural Dynamics and Materials Conference*, Vol. 19, No. April, 2011, pp. 1–13. doi:10.2514/6.2011-2072.
 - [9] Kota, S., Hetrick, J. A., Osborn, R., Paul, D., Pendleton, E., Flick, P., and Tilmann, C., “Design and application of compliant mechanisms for morphing aircraft structures,” *Proc. SPIE*, Vol. 5054, No. November, 2003, pp. 24–33. doi:10.1117/12.483869, URL <http://dx.doi.org/10.1117/12.483869>.
 - [10] Sofla, A., Meguid, S., Tan, K., and Yeo, W., “Shape morphing of aircraft wing: Status and challenges,” *Materials & Design*, Vol. 31, No. 3, 2010, pp. 1284–1292. doi:10.1016/j.matdes.2009.09.011, URL <http://linkinghub.elsevier.com/retrieve/pii/S0261306909004968>.
 - [11] Barbarino, S., Pecora, R., Lecce, L., Concilio, A., Ameduri, S., and Calvi, E., “A novel SMA-based concept for airfoil structural morphing,” *Journal of Materials Engineering and Performance*, Vol. 18, No. 5-6, 2009, pp. 696–705. doi:10.1007/s11665-009-9356-3.
 - [12] Diaconu, C. G., Weaver, P. M., and Mattioni, F., “Concepts for morphing airfoil sections using bi-stable laminated composite structures,” *Thin-Walled Structures*, Vol. 46, No. 6, 2008, pp. 689–701. doi:10.1016/j.tws.2007.11.002.
 - [13] Daynes, S., Nall, S., Weaver, P., Potter, K., Margaris, P., and Mellor, P., “Bistable Composite Flap for an Airfoil,” *Journal of Aircraft*, Vol. 47, No. 1, 2010, pp. 334–338. doi:10.2514/6.2009-2103, URL <http://arc.aiaa.org/doi/abs/10.2514/6.2009-2103>.
 - [14] Rivas-Padilla, J., Arrieta, A. F., and Boston, D. M., “Design of selectively compliant morphing structures with shape-induced bi-stable elements,” *AIAA Scitech 2019 Forum*, 2019. doi:10.2514/6.2019-0855.
 - [15] Larson, R. R., “Flight Control System Development and Flight Test Experience With the F-111 Mission Adaptive Wing Aircraft,” Tech. rep., NASA Ames Research Center, Edwards, California, 1986.
 - [16] Kudva, J. N., “Overview of the DARPA Smart Wing Project,” *Journal of Intelligent Materials Systems and Structures*, Vol. 15, No. 4, 2004, pp. 261–267. doi:10.1177/1045389X04042796.
 - [17] Molinari, G., Quack, M., Dmitriev, V., Morari, M., Jenny, P., and Ermanni, P., “Aero-Structural Optimization of Morphing Airfoils for Adaptive Wings,” *Journal of Intelligent Material Systems and Structures*, Vol. 22, No. 10, 2011, pp. 1075–1089. doi:10.1177/1045389X11414089, URL <http://jim.sagepub.com/content/22/10/1075://jim.sagepub.com/content/22/10/1075.full.pdf://jim.sagepub.com/content/22/10/1075.short>.
 - [18] Rivero, A. E., Fournier, S., Weaver, P. M., Cooper, J. E., and Woods, B. K. S., “Manufacturing and characterisation of a composite FishBAC morphing wind tunnel model,” *ICAST 2018: 29th International Conference on Adaptive Structures and Technologies*, Seoul, Republic of Korea, 2018, pp. 1–14.
 - [19] Rivero, A. E., Weaver, P., and Woods, B. K., “Structural Modelling of Compliance-Based Morphing Structures under Transverse Shear Loading,” *AIAA SciTech 2019 Forum*, American Institute of Aeronautics and Astronautics, San Diego, CA, 2019. doi:10.2514/6.2019-0229, URL <https://arc.aiaa.org/doi/10.2514/6.2019-0229>.
 - [20] Woods, B. K. S., and Friswell, M. I., “Preliminary Investigation of a Fishbone Active Camber Concept,” *ASME Conference on Smart Materials, Adaptive Structures and Intelligent Systems*, 2012. doi:10.1017/CBO9781107415324.004.
 - [21] Rivero, A. E., Weaver, P. M., Cooper, J. E., and Woods, B. K., “Parametric structural modelling of fish bone active camber morphing aerofoils,” *Journal of Intelligent Material Systems and Structures*, 2018, p. 1045389X1875818. doi:10.1177/1045389X18758182, URL <http://journals.sagepub.com/doi/10.1177/1045389X18758182>.
 - [22] Tang, A. Y., and Amin, N., “Some Numerical Approaches to Solve Fluid Structure Interaction Problems in Blood Flow,” *Abstract and Applied Analysis*, Vol. 2014, 2014, pp. 1–8. doi:10.1155/2014/549189.
 - [23] Sieber, G., “Numerical Simulation of Fluid-Structure Interaction Using Loose Coupling Methods,” Ph.D. thesis, 2002. URL <http://tuprints.ulb.tu-darmstadt.de/id/eprint/254%5Cnhttp://tuprints.ulb.tu-darmstadt.de/254>.

- [24] Krawczyk, P., Beyene, A., and MacPhee, D., "Fluid structure interaction of a morphed wind turbine blade," *International Journal of Energy Research*, Vol. 37, 2013, pp. 1784–1793. doi:10.1002/er.
- [25] MacPhee, D. W., and Beyene, A., "Fluid-structure interaction analysis of a morphing vertical axis wind turbine," *Journal of Fluids and Structures*, Vol. 60, 2016, pp. 143–159. doi:10.1016/j.jfluidstructs.2015.10.010, URL <http://dx.doi.org/10.1016/j.jfluidstructs.2015.10.010>.
- [26] Oehler, S. D., Hartl, D. J., Turner, T. L., and Lagoudas, D. C., "Modeling fluid structure interaction with shape memory alloy actuated morphing aerostructures," *Proc. SPIE 8343, Industrial and Commercial Applications of Smart Structures Technologies*, San Diego, CA, 2012, p. 834305. doi:<https://doi.org/10.1117/12.918061>.
- [27] Heo, H., Ju, J., and Kim, D. M., "Compliant cellular structures: Application to a passive morphing airfoil," *Composite Structures*, Vol. 106, 2013, pp. 560–569. doi:10.1016/j.compstruct.2013.07.013, URL <http://dx.doi.org/10.1016/j.compstruct.2013.07.013>.
- [28] Barlas, A. K., and Akay, B., "Optimization of morphing flaps based on fluid structure interaction modeling," *AIAA SciTech Forum*, Kissimmee, Florida, 2018, pp. 1–15. doi:10.2514/6.2018-0998.
- [29] De Gaspari, A., Ricci, S., and Riccobene, L., "Design, Manufacturing and Wind Tunnel Validation of an Active Camber Morphing Wing Based on Compliant Structures," *25th International Conference on Adaptive Structures and Technologies (ICAST 2014)*, 2014, pp. 1–12. doi:10.2514/6.2016-1316, URL http://library.eawag-empa.ch/icast_proceedings_2014_open_access/ICAST2014062.pdf.
- [30] Miller, S. C., Rumpfkeil, M. P., and Joo, J. J., "Fluid-Structure Interaction of a Variable Camber Compliant Wing," *AIAA SciTech Forum*, 2015, pp. 1–12. doi:10.2514/6.2015-1235.
- [31] Fasel, U., Keidel, D., Molinari, G., and Ermanni, P., "Aeroservoelastic Optimization of Morphing Airborne Wind Energy Wings," *AIAA Scitech 2019 Forum*, San Diego, CA, 2019. doi:10.2514/6.2019-1217.
- [32] Daynes, S., and Weaver, P. M., "Morphing Blade Fluid-Structure Interaction," *53rd AIAA/ASME/ASCE/AHS/ASC Structures, Structural Dynamics and Materials Conference*, Honolulu, Hawaii, 2012. doi:10.2514/6.2012-1667.
- [33] Woods, B. K. S., Dayyani, I., and Friswell, M. I., "Fluid/Structure-Interaction Analysis of the Fish-Bone-Active-Camber Morphing Concept," *Journal of Aircraft*, Vol. 52, No. 1, 2014, pp. 307–319. doi:10.2514/1.C032725, URL <https://doi.org/10.2514/1.C032725>.
- [34] Woods, B. K. S., and Friswell, M. I., "Multi-objective geometry optimization of the Fish Bone Active Camber morphing airfoil," *Journal of Intelligent Material Systems and Structures*, Vol. 27, No. 6, 2016, pp. 808–819. doi:10.1177/1045389X15604231.
- [35] Dixon, K., Simão Ferreira, C. J., Hofemann, C., Van Bussel, G., and Van Kuik, G., "A 3D unsteady panel method for vertical axis wind turbines," *European Wind Energy Conference and Exhibition 2008*, Vol. 6, Brussels, Belgium, 2008, pp. 2981–2990. URL <http://www.scopus.com/inward/record.url?eid=2-s2.0-84870029758&partnerID=tZ0tx3y1>.
- [36] Pinzón, S., "Introducción a la teoría VLM (Vortex Lattice Theory)," *Ciencia y Poder Aéreo*, Vol. 10, No. 1, 2017, p. 39. doi:10.18667/cienciaypoderaereo.433, URL <http://dx.doi.org/10.18667/cienciaypoderaereo.433>.
- [37] Owens, D., "Weissinger's model of the nonlinear lifting-line method for aircraft design," *36th AIAA Aerospace Sciences Meeting and Exhibit*, American Institute of Aeronautics and Astronautics, 1998, pp. 1–10. doi:10.2514/6.1998-597.
- [38] Sivells, J. C., and Neely, R. H., "Method for Calculating Wing Characteristics by Lifting-Line Theory using Nonlinear Section Lift Data," *NASA Technical Note No. 1269*, 1947.
- [39] Anderson, J., Corda, S., and Van Wie, D., "Numerical lifting line theory applied to drooped leading-edge wings below and above stall," *Journal of Aircraft*, Vol. 17, No. 12, 1980, pp. 898–904. doi:10.2514/3.44690, URL <http://arc.aiaa.org/doi/10.2514/3.44690>.
- [40] Şugar Gabor, O., Koreanschi, A., and Botez, R. M., "A new non-linear vortex lattice method: Applications to wing aerodynamic optimizations," *Chinese Journal of Aeronautics*, Vol. 29, No. 5, 2016, pp. 1178–1195. doi:10.1016/j.cja.2016.08.001.
- [41] Şugar-Gabor, O., Koreanschi, A., and Ruxandra, M. R., "An efficient numerical lifting line method for practical wing optimization through morphing on the Hydra Technologies UAS-S4," *CASI AERO 2013 Conference*, Toronto, Canada, 2013, pp. 1–11. doi:10.1109/AINA.2014.46.
- [42] Chadwick, E., "A slender-wing theory in potential flow," *Proceedings of the Royal Society A: Mathematical, Physical and Engineering Sciences*, Vol. 461, No. 2054, 2005, pp. 415–432. doi:10.1098/rspa.2004.1295.
- [43] Katz, J., and Plotkin, A., *Low-Speed Aerodynamics: From Wing Theory to Panel Methods*, McGraw-Hill, Singapore, 1991.
- [44] Phillips, W. F., and Snyder, D. O., "Modern Adaptation of Prandtl's Classic Lifting-Line Theory," *Journal of Aircraft*, Vol. 37, No. 4, 2000, pp. 662–670. doi:10.2514/2.2649, URL <http://arc.aiaa.org/doi/10.2514/2.2649>.

- [45] Drela, M., "XFOIL: An Analysis and Design System for Low Reynolds Number Airfoils," *Lecture Notes in Engineering*, edited by T. Mueller, Springer, Berlin, Heidelberg, 1989, 54th ed., pp. 1–12. doi:10.1007/978-3-642-84010-4{_}1.
- [46] Fournier, S., and Woods, B. K., "Surrogate Model of Fish Bone Active Camber concept," *AIAA Scitech 2019 Forum*, American Institute of Aeronautics and Astronautics, San Diego, CA, 2019, pp. 1–12. doi:10.2514/6.2019-1859.
- [47] Mason, W., *Appendix A: Geometry for Aerodynamicists*, Virginia Polytechnic Institute and State University, 1997. URL http://www.dept.aoe.vt.edu/~mason/Mason_f/CAtxtAppA.pdf.
- [48] Whitney, J. M., *Structural Analysis of Laminated Anisotropic Plates*, Technomic Publishing, Lancaster, Pennsylvania, 1987.
- [49] Ilanko, S., Monterrubio, L., and Mochida, Y., *The Rayleigh-Ritz Method for Structural Analysis*, Iste Series, Wiley, London and New York, 2015.
- [50] Hyer, M. H., *Stress Analysis of Fiber-Reinforced Composite Materials*, McGraw-Hill, New Delhi, 2014.
- [51] Coburn, B. H., "Buckling of stiffened variable stiffness panels," Ph.D. thesis, University of Bristol, 2015.
- [52] Jaunky, N., Knight, N., and Ambur, D., "Buckling of arbitrary quadrilateral anisotropic plates," *AIAA Journal*, Vol. 33, No. 5, 1995, pp. 938–944. doi:10.2514/3.12512, URL <http://dx.doi.org/10.2514/3.12512>.
- [53] Groh, R. M., and Weaver, P. M., "Static inconsistencies in certain axiomatic higher-order shear deformation theories for beams, plates and shells," *Composite Structures*, Vol. 120, 2015, pp. 231–245. doi:10.1016/j.compstruct.2014.10.006, URL <http://dx.doi.org/10.1016/j.compstruct.2014.10.006>.
- [54] Mansfield, E. H., *The Bending and Stretching of Plates*, 2nd ed., Cambridge University Press, 1989. URL <http://dx.doi.org/10.1017/CB09780511525193>.
- [55] Wu, Z., Raju, G., and Weaver, P. M., "Framework for the Buckling Optimization of Variable-Angle Tow Composite Plates," *AIAA Journal*, Vol. 53, No. 12, 2015, pp. 3788–3804. doi:10.2514/1.J054029, URL <http://arc.aiaa.org/doi/abs/10.2514/1.J054029>.
- [56] Woods, B. K. S., and Friswell, M. I., "Fluid-Structure Interaction Analysis of the Fish Bone Active Camber Mechanism," *54th AIAA/ASME/ASCE/AHS/ASC Structures, Structural Dynamics, and Materials Conference*, Boston, Massachusetts, 2013, pp. 1–15.
- [57] Craft, T., *Numerical Solution of Equations*, The University of Manchester, Manchester, UK, 2008.
- [58] Ferziger, J. H., and Peric, M., *Computational Methods for Fluid Dynamics*, 3rd ed., Springer-Verlag Berlin Heidelberg, 2002. doi:10.1007/978-3-642-56026-2.
- [59] Barron, R. M., and Neyshabouri, A. A. S., "Effects of under-relaxation factors on turbulent flow simulations," *International Journal for Numerical Methods in Fluids*, Vol. 42, 2003, pp. 923–928.
- [60] Tornero, G., "Non-Linear Weissinger Lifting-Line Model for Preliminary 3D Aerodynamic Analysis of Morphing Wings," *Masters of Engineering Project. University of Bristol*, 2017, pp. 1–22.
- [61] Deperrois, A., "Guidelines for XFLR5: Analysis of foils and wings operating at low Reynolds numbers," , No. February, 2013, pp. 1–72. URL <http://scholar.google.com/scholar?hl=en&btnG=Search&q=intitle:Analysis+of+foils+and+wings+operating+at+low+Reynolds+numbers#0>.
- [62] Smith, S. C., "A Computational and Experimental Study of Nonlinear Aspects of Induced Drag," *NASA Report No 3598*, 1996. URL <http://www.csa.com/partners/viewrecord.php?requester=gs&collection=TRD&recid=N9621664AH>.
- [63] Rivero, A. E., Weaver, P. M., Cooper, J. E., and Woods, B. K., "Progress on the Design , Analysis and Experimental Testing of a Composite Fish Bone Active Camber Morphing Wing," *ICAST 2017: 28th International Conference on Adaptive Structures and Technologies*, Cracow, Poland, 2017, pp. 1–11.
- [64] Cook, M. V., *Static Equilibrium and Trim*, 2nd ed., Butterworth-Heinemann, 2013. doi:10.1016/B978-0-08-098242-7.00003-1, URL <https://www.sciencedirect.com/science/article/pii/B9780080982427000031>.
- [65] Lotov A.V., M. K., *Visualizing the Pareto Frontier. In: Branke J., Deb K., Miettinen K., Słowiński R. (eds) Multiobjective Optimization. Lecture Notes in Computer Science*, Springer, Berlin, Heidelberg, 2008. doi:https://doi.org/10.1007/978-3-540-88908-3{_}9.